Modeling of SOFC Running on Partially Pre-reformed Gas Mixture

Meng Ni*

Building Energy Research Group, Department of Building and Real Estate

The Hong Kong Polytechnic University, Hung Hom, Kowloon, Hong Kong

Abstract

A two dimensional model is developed to study the transport and reaction processes in solid oxide fuel cells (SOFCs) fueled by partially pre-reformed gas mixture, considering the direct internal reforming (DIR) of methane and water gas shift (WGS) reaction in the porous anode of SOFC. Electrochemical oxidations of H_2 and CO fuels are both considered. The model consists of an electrochemical, a chemical model, and a computational fluid dynamics (CFD) model. Two chemical models are compared to examine their effects on SOFC modeling results. Different from the previous studies on hydrogen fueled SOFC, higher gas velocity is found to slightly decrease the performance of SOFC running on pre-reformed gas mixture, due to suppressed gas composition variation at a higher gas velocity. The current density distribution along the gas channels at an inlet temperature of 1173K is quite different from that at 1073K, as DIR reaction is facilitated at a higher temperature. It is also found that neglecting the electrochemical oxidation of CO can considerably underestimate the total current density of SOFC running on pre-reformed hydrocarbon fuels. An alternative method is proposed to numerically determine the open-circuit potential of SOFC running on hydrocarbon fuels. Electrochemical reactions are observed at open-circuit potentials.

Keywords: *SOFC; Ceramic Fuel Cells; Direct Internal Reforming; Water Gas Shift Reaction; Modeling; Mixed potential*

---

* Corresponding author. Tel. +852 2766 4152; Fax: 852 2764 5131
Email: bsmengni@inet.polyu.edu.hk (M. Ni)

1. Introduction

Solid oxide fuel cells (SOFCs) employing ceramic electrolytes are promising electrochemical devices, that convert the chemical energy of fuels into electricity in an efficient, clean and quiet manner. SOFCs are usually operated at higher temperatures (i.e. 1073K) in order to achieve good ionic conductivity of the electrolyte, like yttrium-stabilized-zirconia (YSZ) [1,2]. The high temperature makes SOFC suitable for cogeneration, as the waste heat from SOFC can be recovered by integrating with other thermodynamic cycles [3-6]. Besides, carbon monoxide (CO), a poisoning gas for low temperature fuel cells (i.e. proton exchange membrane fuel cell: PEMFC) [7], can be used as a fuel in an SOFC. Therefore, alternative fuels, like methane, methanol, and ethanol, can be used in SOFCs for power generation [8-10].

As a key component of natural gas and biogas, methane (CH_4) has been extensively studied as a model fuel for SOFC [11]. For fuel cell applications, CH_4 needs to be steam reformed either internally or externally, as the electrochemical oxidation of methane in SOFC is difficult. External reforming requires additional fuel processors and thus adds to the total cost and complexity of the system. However, the operating parameters can be easily adjusted to obtain desired gas composition to favor electrochemical reactions in SOFC [12-14]. For comparison, direct internal reforming (DIR) of methane in SOFC eliminates the need of external fuel processors and thus reduces the system cost and complexity [15-20]. However, the occurrence of chemical reactions (endothermic DIR and exothermic water gas shift reaction: WGSR) complicate the SOFC temperature field and more importantly, carbon deposition can occur in an SOFC with DIR and WGS, which in turn can degrade the SOFC performance substantially [21]. Besides, both DIR and WGS reactions require steam in the anode, which can dilute the fuel concentration and reduce the SOFC performance [22, 23]. In a recent study, it is found that running on methane/steam mixture without external reforming, the electrolytic effect is observed in an SOFC, at an operating potential

of 0.8V [24]. This electrolytic effect in SOFC is due to the non-uniform electrolyte Nernst potential and uniform operating potential along the SOFC channel. In this paper, the previously developed models [25,26] are extended to study the coupled transport and reaction phenomena in an SOFC running on partially pre-reformed methane fuel. Different from the previous studies that only consider electrochemical oxidation of H_2 fuel, the electrochemical oxidation of CO fuel is included in the model. Two chemical models used for simulating the kinetics of DIR and WGS are compared. The effects of flow rate, inlet temperature, and operating potential on SOFC performance are investigated. An alternative method is proposed to find the open circuit potential of SOFC considering electrochemical reactions of both H_2 and CO fuels. The current density distribution in SOFC at open-circuit potentials are presented and discussed.

2. Model Development

In this study, the partially pre-formed methane gas mixture is used in SOFC for power generation. Typical gas composition at the anode inlet are 17.1% CH_4, 2.9% CO, 49.3% H_2O, 26.3% H_2, and 4.4% CO_2, respectively [27]. The computational domain and working mechanism in a planar SOFC is shown in Figure 1, including the two interconnectors, the fuel gas channel, porous anode, dense electrolyte, porous cathode, and air gas channel. Typical dimensions of the gas channel and the cell component thickness are used in the modeling study and summarized in Table 1.

In operation, the partially pre-reformed methane fuel and air are supplied to the anode and cathode channels, respectively. In the anode catalyst layer, DIR reaction (Eq. 1) and WGS reaction (Eq.2) take place, producing hydrogen fuel.

$$CH_4 + H_2O \leftrightarrow CO + 3H_2 \quad (1)$$

$$CO + H_2O \leftrightarrow CO_2 + H_2 \quad (2)$$

The H_2 molecules diffuse through the porous anode layer to the triple-phase-boundary (TPB) at the electrolyte-anode interface, where H_2 molecules react with oxygen ions (O^{2-}) to produce H_2O and electrons (Eq. 3). The electrons produced are transported to the cathode via an external circuit to produce useful power. At the cathode side, O_2 molecules diffuse through the porous cathode to the TPB at the electrolyte-cathode interface and react with electrons that come from the anode to produce oxygen ions (Eq. 4), which are subsequently transported through the dense electrolyte to the anode side.

$$H_2 + O^{2-} \rightarrow H_2O + 2e^- \tag{3}$$

$$0.5O_2 + 2e^- \rightarrow O^{2-} \tag{4}$$

In addition to H_2, CO can also participate in electrochemical reaction for power generation,

$$CO + O^{2-} \rightarrow CO_2 + 2e^- \tag{5}$$

The electrochemical oxidation of CH_4 is neglected, as the electrochemical oxidation rate of CH_4 is very small compared with DIR and WGS reactions [28,29]. In addition, chemical reaction of CO_2 with CH_4 is neglected. With the above-mentioned working mechanisms and assumptions, a 2D model is developed to study the coupled transport and chemical/electrochemical reactions in a planar SOFC running on partially pre-reformed methane gas mixture. The model consists of an electrochemical model, a chemical model and a computational fluid dynamics (CFD) model.

2.1 Electrochemical Model

The electrochemical model is used to calculate the local current density (J) at given operating potential (V). In an SOFC, the interconnector is used to define the configuration of flow channel and collect the current produced. Due to its high electrical conductivity, it is reasonable to

assume that the operating potential does not vary along the flow channel. Based on the previous studies, the *J-V* relationship of an SOFC in operation can be obtained as [30,31],

$$V = E - \eta_{act,a} - \eta_{act,c} - \eta_{ohmic} \tag{6}$$

$$E_{H_2} = 1.253 - 0.00024516T + \frac{RT}{2F}\ln\left[\frac{P_{H_2}^I \left(P_{O_2}^I\right)^{0.5}}{P_{H_2O}^I}\right] \tag{7}$$

$$E_{CO} = 1.46713 - 0.0004527T + \frac{RT}{2F}\ln\left[\frac{P_{CO}^I \left(P_{O_2}^I\right)^{0.5}}{P_{CO_2}^I}\right] \tag{8}$$

where E is the equilibrium potential (Nernst potential) and the subscripts H_2 and CO represent the equilibrium potential associated with H_2 and CO fuels, T is temperature (K); η_{ohmic} is the ohmic overpotential; $\eta_{act,a}$ and $\eta_{act,c}$ are the activation overpotentials at the anode and cathode, respectively; R is the universal gas constant (8.3145 J.mol^{-1}K^{-1}); and F is the Faraday constant (96485 C.mol^{-1}). P^I is the partial pressure at the electrode-electrolyte interface, which means that the concentration overpotentials are included in the Nernst potential (E). The Ohm's law is used to calculate the ohmic overpotential. As the activation overpotential and current density usually follow a linear relationship according to experimental observations [32], the activation overpotentials are calculated as [33],

$$\eta_{act} = \frac{RTJ}{2FJ_0} \tag{9}$$

where J_0 is exchange current density (A.m^{-2}) of the electrode. According to the previous studies [33], $J_{0,a}$ = 5300 A.m^{-2} and $J_{0,c}$ = 2000 A.m^{-2} are used for anode and cathode, respectively. For CO electrochemical oxidation, there are very limited experimental data available in the literature. Matsuzaki and Yasuda [28] experimentally measured the electrochemical oxidation rates of H_2 and CO at the interface of porous Ni-YSZ cermet anode and YSZ electrolyte. It was found that the

electrochemical oxidation rate of H_2 was 1.9-2.3 times and 2.3-3.1 times higher than that of CO at 1023 and 1273K, respectively [28]. Thus, the exchange current density for H_2 electrochemical oxidation is assumed to be 2.5 times that for CO electrochemical oxidation. Accordingly, the value of $J_{0,a}$ for CO electrochemical oxidation is assumed to be $0.4\times 5300 A.m^{-2}$, that is, 2120 A.m^{-2}. It should also be noted that the value of $J_{0,a}$ can be easily adjusted once more reliable experimental data are available.

2.2. Chemical model

The chemical model is developed to calculate the rates of DIR and WGS reactions and the related rates of heat consumption/generation. In the literature, the rates (mol.m^{-3}.s^{-1}) of DIR and WGS reactions are usually calculated using the formulas proposed by Lehner et al. [34] or by Haberman and Young [35]. Their models are summarized in Table 2.

The enthalpy changes for endothermic DIR and exothermic WGS reactions are used to determine the heat generation/consumption due to the chemical reactions [36]. Considering the dependence of enthalpy on temperature, the reaction heat (J.mol^{-1}) for DIR and WGS reaction can be approximately calculated as,

$$H_{DIR} = -\left(206205.5 + 19.5175T\right) \tag{10}$$

$$H_{WGS} = 45063 - 10.28T \tag{11}$$

2.3. Computational fluid dynamics (CFD) model

In an SOFC, fluid flow, heat transfer and mass transfer occur simultaneously. The fluid flow in the gas channels of an SOFC is typically laminar due to a low Reynolds number. The governing equations for mass conservation, momentum conservation, energy conservation, and their corresponding source terms are summarized in Table 3 [37,38].

In Table 3, U and V are the velocity components in x and y directions; ρ and μ are the gas density and viscosity of the gas mixture respectively, which depends on local temperature and gas composition. Y_i denotes the mass fraction of species i. $D_{i,m}^{eff}$ is the effective diffusion coefficient of species i in gas mixture (both anode and cathode). k ($W.m^{-1}.K^{-1}$) and c_p ($J.kg^{-1}.K^{-1}$) are the thermal conductivity and heat capacity respectively. The subscripts f and s represents fluid and solid, respectively.

The mass fraction of species i (Y_i) can be calculated based on the molar fraction (X_i) and molecular weight (M_i) of species i,

$$Y_i = X_i \left(\frac{M_i}{\sum_{i=1}^{N} X_i M_i} \right) \tag{12}$$

The effective diffusion coefficient of species i ($D_{i,m}^{eff}$) in gas mixture can be evaluated as;

$$\frac{1}{D_{i,m}^{eff}} = \frac{\xi}{\varepsilon} \left(\frac{\sum_{j \neq i} \frac{X_j}{D_{ij}}}{1 - X_i} + \frac{3}{2 r_p} \sqrt{\frac{\pi M_i}{8RT}} \right) \tag{13}$$

$$D_{ij} = \frac{0.0026 T^{1.5}}{p \sqrt{\frac{2 M_i M_j}{M_j + M_i}} \left(\frac{\sigma_i + \sigma_j}{2} \right)^2 \Omega_D} \tag{14}$$

$$\Omega_D = \frac{1.06036}{\left(\frac{k_b T}{\varepsilon_{i,j}} \right)^{0.1561}} + \frac{0.193}{\exp\left(0.47635 \left(\frac{k_b T}{\varepsilon_{i,j}} \right) \right)} + \frac{1.03587}{\exp\left(1.52996 \left(\frac{k_b T}{\varepsilon_{i,j}} \right) \right)} + \frac{1.76474}{3.89411 \left(\frac{k_b T}{\varepsilon_{i,j}} \right)} \tag{15}$$

where ξ / ε is the ratio of tortuosity to porosity of porous electrodes; and r_p is the radius of pores. D_{ij} is the binary diffusion coefficient of species i and j. σ is the mean characteristic length of species and Ω_D is a dimensionless diffusion collision. k_b is the Boltzmann's constant

($1.38066\times10^{-23}\left(\mathrm{J.K^{-1}}\right)$). The values of σ_i and $\varepsilon_{i,j}$ used in the present study are summarized in Table 4 [39].

The source term S_m in continuity equation represents the mass change due to electrochemical reactions. Since electrochemical reactions are assumed to occur only at the electrode-electrolyte interface, the source term is non-zero at the electrode-electrolyte interface only and zero in other regions. In Table 3, A_{act} is the active area for electrochemical reaction at the electrode-electrolyte interface and V_c is the size of control volume. Δy is the width of the control volume in y direction at the electrode-electrolyte interface. The negative sign for the cathode means the mass (oxygen) is electrochemically consumed. The Darcy's law is used as source terms (S_x and S_y) in momentum equations (Table 3) so that the momentum equations are valid for both the gas channels and the porous electrodes [24, 26]. The source term (S_T, $\mathrm{W.m^{-3}}$) in energy equation includes: (1) heat generation due to electrochemical entropy change (ΔS, $\mathrm{J.K^{-1}.mol^{-1}}$) and irreversible overpotentials (η_t); (2) heat energy consumption by DIR reaction (Eq. 1); and heat generation due to WGS reaction (Eq. 2). In the porous anode, both DIR and WGS contribute to the heat source term (S_T). In the dense electrolyte, the source term (S_T) includes the irreversible loss through entropy change and the total overpotentials. The similar procedure for S_m (source term for continuity equation) can be adopted for calculating the source terms (S_{sp}) in species equations, with inclusion of the DIR and WGS reactions in the porous anode.

3. Numerical Methodology

The finite volume method (FVM) is used to discretize and solve the governing equations [37]. The boundary conditions and the detailed calculation procedures can be found in the previous publication [24, 26]. The iteration scheme is shown in Figure 2. In each iteration, electrochemical

and chemical models are solved to calculate the current densities (related to the rates of electrochemical reactions) and the rate of chemical reactions (DIR and WGS reactions), which are then used to determine the source terms in the CFD model. Subsequently, the CFD equations are computed to update the temperature field, velocity field and gas composition distribution in SOFC, which are used to solve the electrochemical and the chemical models again. Computation is repeated until convergence is obtained. The in-house CFD code is written in FORTRAN.

4. Results and Discussion

Before parametric simulation, the model developed must be validated. As the electrochemical model, chemical model and the CFD model have been validated respectively in the previous publications [24,26], the validation of the models is not repeated here. The dimensions and typical structural/operating parameters used are summarized in Table 1.

4.1. Comparison of different chemical models

In the literature, both the Lehnert et al.'s model [34] and Haberman and Young's model [35] are used to calculate the DIR and WGS reaction rates. Figure 3 compares the calculated rates for DIR and WGS reactions using these two chemical models, at an inlet temperature of 1073K and an operating potential of 0.8V. Both DIR and WGS reaction rates are the highest at the inlet and decrease in the downstream of the gas flow channels. The Lehnert et al's model predicts the DIR reaction rates to decrease from about 19.3 $mol.m^{-3}.s^{-1}$ at the inlet to about 9 $mol.m^{-3}.s^{-1}$ at the outlet (Fig. 3a). The calculated DIR reaction rates are on the same order but a little lower than the data by Lehnert et al. [34]. This is due to a lower simulation temperature is used in the present study than that in Lehnert et al.'s study [34]. For comparison, Haberman and Young's model results in a lower rates and smaller variation of DIR reaction along the gas flow channel (Fig. 3b). The WGS reaction

rates predicted by Lehnert et al. decrease from about 5.75 $mol.m^{-3}.s^{-1}$ at the SOFC inlet to about – 3.3 $mol.m^{-3}.s^{-1}$ at the outlet (Fig. 3c). The negative reaction rates near the outlet means the direction of WGS reaction (Eq. 2) is reversed. In other words, CO_2 and H_2 are consumed to produce H_2O and CO near the outlet of SOFC. Compared with Lehnert et al.'s model, the Haberman and Young's model predicts the WGS reaction rates to decrease from about 4.88 $mol.m^{-3}.s^{-1}$ at the SOFC inlet to about – 3.84 $mol.m^{-3}.s^{-1}$ at the outlet (Fig. 3d).

Figure 4 compares the gas composition in SOFC using different chemical models. Due to higher rates of DIR reaction, the variation in gas composition is larger for Lehnert et al's model than the Haberman and Young's model. Using the Lehnert et al's model, the CH_4 molar fraction is found to decrease from 0.171 at the SOFC inlet to be less than 0.1 at the outlet (Fig. 4a). For comparison, the CH_4 molar fraction is still higher than 0.12 at the SOFC outlet using the Haberman and Young's model (Fig. 4b). In addition, the increase in H_2 molar fraction along the SOFC gas channel is higher using Lehnert et al's model (from 0.263 to 0.34) than using Haberman and Young's model (from 0.263 to 0.296), as can be seen from Fig. 4c and 4d. The variation of CO molar fraction in SOFC is small for both chemical models (Fig. 4e and 4f). Using the Lehnert et al's model, slight increase in CO molar fraction is observed due to high DIR reaction rates (Fig. 4e). For comparison, the CO molar fraction is found to decrease slightly in the SOFC (Fig. 4f), indicating the rate of CO generation is slightly lower than the rate of CO electrochemical oxidation. Consequently, the current density predicted using Lehnert et al.'s model is found higher than that using the Haberman and Young's model. The current density contributed by CO fuel is smaller than that by H_2 fuel, as H_2 fuel is electrochemically oxidized faster than CO fuel.

The results presented above show that the calculated reaction rates could be quite different when different chemical models are used. Thus, the gas composition may exhibit different variation pattern in the SOFC. However, to evaluate which model is more accurate, detailed and systematic

experimental measurement and validation are needed, which is out of the scope of the present study. In the subsequent simulations, the Haberman and Young's model is used for calculating the rates of DIR and WGS reactions.

4.2. Effect of inlet temperature

The effect of inlet temperature on performance of the SOFC is shown in Fig. 6. It is found that the current densities associated with both H_2 fuel and CO fuel increase with increasing inlet temperature, indicating that higher electric power generation can be obtained at a higher inlet temperature. More importantly, the current density distributions in SOFC are quite different at different temperatures. At an inlet temperature of 1073K, the current densities decrease slightly along the gas flow channel. For comparison, the current densities at a high temperature (1173K) increase considerably near the inlet and become almost invariant in the downstream of the SOFC. The difference is mainly caused by the different distributions in molar fractions of H_2 and CO in the anode. At an inlet temperature of 1173K, the molar fractions of H_2 and CO (Figs. 7a and 7b) are both higher than those at 1073K (Figs. 4d and 4f), mainly because of considerably higher rate of DIR reaction at 1173K (Fig. 7c) than that at 1073K (Fig. 3b). The effect of WGS reaction on gas composition and current density is insignificant since the reaction rate is small (Fig. 7d). As a result, the molar fractions of H_2 and CO increase with increasing temperature, leading to higher current densities (Fig. 6).

In addition, the inlet temperature also considerably influences the SOFC temperature field. At a high inlet temperature (1173K), the temperature in SOFC is decreased quickly from 1173K to about 1154K near the inlet, followed by gradual increase to about 1167K in the downstream (Fig. 7e). For comparison, at an inlet temperature of 1073K, only slight increase in temperature (about 1K) along the gas flow channel is observed. At a high temperature (1173K), the rate of DIR

reaction is high near the inlet and consuming more heat there, leading to considerable decrease in temperature. In the downstream, the heat production by irreversible overpotential losses due to relatively high current density exceeds the heat consumption by DIR reaction, leading to an increase in temperature along the gas channel. At a low inlet temperature (1073K), variation in temperature is small due to low rates of DIR and WGS reactions and low current densities.

4.3. Effect of inlet gas velocity

Figure 8 compares the electrochemical performance of SOFC running on pre-reformed methane fuel at different inlet gas velocities. It is found that increasing the inlet gas velocity decreases the current densities of SOFC. This is different from the previous study on hydrogen fueled SOFC, in which increased current density is achieved at high inlet gas velocity [26]. When H_2 is used as a fuel, the H_2 molar fraction decreases and H_2O molar fraction increases along the gas flow channel due to electrochemical oxidation of H_2. An increase in gas velocity helps sustain high molar fraction of H_2 in the downstream, thus leading to an increase in current density. In the present study, both DIR and WGS reactions favor H_2 production (Eq. 1 and 2), leading to increased H_2 molar fraction along the gas flow channel. However, a higher gas velocity tends to suppress the variation of gas composition along the channel (Fig. 9a), leading to smaller increase in H_2 molar fraction than that at a lower gas velocity (Fig. 7a). Similarly, the variation of CO molar fraction is reduced as well at higher gas velocity (Fig. 9b) than at lower velocity (Fig. 7b).

The reaction rates at the inlet are the same for both low inlet gas velocity (anode: $0.5 m.s^{-1}$) and high inlet gas velocity case (anode: $1.0 m.s^{-1}$), as can be seen from Figs 7c, 7d, 9c, and 9d. However, smaller reduction in rates of DIR and WGS reactions in the downstream of the gas flow channel is observed at higher inlet gas velocity (anode: $1.0 m.s^{-1}$), mainly due to less variation in gas composition along the channel. Although high velocity tends to sustain uniform temperature

distribution, the heat consumption by DIR reaction is high at a high gas velocity, leading to decreased SOFC temperature (Fig. 9e).

4.4. Effect of operating potential

The distributions of current densities along the gas flow channels at typical operating potentials (0.4V, 0.6V, and 0.8V) are shown in Fig. 10. As expected, the current densities by H_2 fuel and CO fuel are increased with decreasing potential (Fig. 10b and 10c), so does the total current density (Fig. 10a).

The higher current density at lower potential consumes more H_2 and CO fuels, which favors DIR reaction (produces H_2 and CO) and the backward reaction of WGSR (produces CO but consumes H_2), as can be seen from Fig. 11c and 11d. As a result, the H_2 molar fraction in SOFC running on pre-reformed CH_4 fuel does not decrease as the potential is decreased from 0.8V to 0.4V (Fig. 11a), which is different from H_2 fueled SOFC (H_2 molar fraction is decreased with decreasing potential) [26]. In addition, the molar fraction of CO is increased along the gas flow channel and reaches the highest at the middle of SOFC, and decreases in the downstream (Fig. 11b). This indicates the production of CO by DIR reaction and backward WGS reaction exceeds the consumption of CO by electrochemical reaction in the upstream, but the consumption of CO exceeds CO production in the downstream. Compared with operating potential of 0.8V, the temperature in SOFC increases considerably from 1173K at the SOFC inlet to about 1327K at the SOFC outlet at an operating potential of 0.4 (Fig. 11e). The substantial temperature increase means that the heat generation by electrochemical reaction and backward WGS reaction considerably exceeds heat consumption by DIR reaction.

4.5. Effect of CO electrochemical oxidation

In the literature, most of the existing studies only consider electrochemical oxidation of H_2 and assume the rate of electrochemical oxidation of CO to be negligible. Thus it is necessary to examine how does the exclusion of CO electrochemical oxidation influence the predicted SOFC performance. In this section, the electrochemical oxidation of CO is purposely neglected for comparison with the results in the previous sections where CO electrochemical oxidation is considered. When electrochemical oxidation of CO is neglected, the total current density is equal to the current density associated with H_2 fuel only. When both H_2 and CO fuel are electrochemically oxidized, current density by both fuels contributes to the total current density (Fig. 12). Therefore, neglecting electrochemical oxidation of CO can under-estimate both the total current density and the power output of SOFC running on hydrocarbon fuels.

It is found that whether electrochemical oxidation of CO is considered or not does not considerably affect the H_2 molar fraction (Fig. 13a), the rate of DIR reaction (Fig. 13c), and the temperature field (Fig. 13e). However, excluding CO electrochemical oxidation considerably influences the distribution of CO molar fraction and rates of WGS reaction, as can be seen from Fig. 13b and 13d. When CO electrochemical oxidation is not considered, CO molar fraction increases along the gas flow channel (Fig. 13b) due to CO production from DIR reaction. Consequently, the WGS reaction rates are higher than that including CO electrochemical oxidation (Fig. 13d and 9d).

4.6. The open-circuit potential of SOFC

In the present study, the reaction and transport phenomena in methane fueled SOFC at open-circuit potential is studied. To the author's best knowledge, it is the first time to look at the SOFC open-circuit potential considering electrochemical reactions of both H_2 and CO fuels. For H_2-fueled SOFC, the open-circuit potential of SOFC can be determined by the Nernst equation. It is also straightforward to calculate the current densities associated with H_2 fuel and CO fuel for an SOFC

running on pre-reformed CH_4 fuel mixture, at a given operating potential. In this way, the total current density can be easily obtained by simply adding the current densities associated with the H_2 and CO fuels. However, the Nernst potential (or open circuit potential) cannot be determined easily since it is related to both H_2 and CO fuels.

It is considered that at an open-circuit potential, the net current density should be zero (no power output). Thus the open-circuit potential can be determined as the potential yielding zero total current density. It is found that at an inlet temperature of 1073 K, the total current densities are about -1263.83 A.m^{-2} and 777.47 A.m^{-2} at operating potential of 1.0V and 0.9V, respectively. Therefore, the open-circuit potential must be between 0.9V and 1.0V. Assuming a linear relationship between the total current density and the potential (of course more computations can be done to get more data to improve the accuracy), the open-circuit potential is found to be about 0.937V at inlet temperature of 1073K (Fig. 14a). However, it should be noted that the open-circuit potential not only depends on the temperature, but also the gas flow rate, inlet gas composition, etc. By adopting the same methodology, the open-circuit potential at an inlet temperature of 1173K is found to be about 0.936V (Fig. 14b).

The distributions of current density in SOFC at open-circuit potentials are shown in Fig. 15. It is found that the total current density varies considerably along the SOFC gas flow channel at inlet temperature of 1073K and 1173K (Fig. 15a, 15c). The current density associated with H_2 is higher than that associated with CO, as the electrochemical reaction of H_2 is faster than that of CO (Fig. 15b, 15d). However, the difference between them is small near the inlet at a high temperature (Fig. 15d). This is because at the simulation condition of 1173K, the Nernst potential associated with CO is lower than that of H_2 (Fig. 15e). Since the open circuit potential is about 0.936V, Higher than the Nernst potentials near the inlet, the upstream of SOFC is thus in electrolysis operation. The larger difference between the local Nernst potential (for CO) and the operating potential

(0.936V) than that for H_2 tends to yield higher current density (negative) for CO. Meanwhile the lower exchange current density for CO than H_2 tends to yield a lower current density for CO than H_2. As a result, the difference in current densities between CO and H_2 is small near the inlet at 1173K (Fig. 15d). The negative total current density means the upstream of SOFC is in electrolysis operation. The positive total current density in the downstream indicates normal fuel cell operation. This phenomenon is caused by the uniform operating potential and non-uniform Nernst potential along the gas flow channel [40]. The uniform operating potential results from the use of current collector with high electric conductivity along the flow channel. The non-uniform Nernst potential is caused by the varying gas composition due to chemical reactions (DIR and WGS reactions) along the gas flow channel at the anode side. If H_2 is used as a fuel at the anode, there should be no electrolytic effect in SOFC at an open-circuit potential, due to the lack of chemical reaction. For SOFC running on other hydrocarbon fuels, both electrolysis and fuel cell operation will always occur simultaneously at the open-circuit potential, as long as chemical reaction are present.

5. Conclusion

A numerical model is developed to study the performance of SOFC running on partially pre-reformed CH_4 fuel mixture, considering both DIR and WGS reactions in the porous anode. Comparisons of two chemical models are made to examine their difference in calculating the rates of DIR and WGS reactions in SOFC anode. It is found that the Lehnert et al's model yields higher rate of DIR reaction near the SOFC inlet than the Haberman and Young's model. For WGS reaction, the rates by Lehnert et al's model gives higher rates for forward reaction and lower rates for backward reaction than the Haberman and Young's model. Accordingly, the molar fraction of H_2 and CO are higher using Lehnert et al's model than the Haberman and Young's model, leading to higher current density of SOFC. When the inlet temperature is increased from 1073K to 1173K, the

current density is considerably increased. This is because the high temperature facilitates DIR reaction and increases the molar fraction of H_2 and CO.

Different from H_2-fueled SOFC, the present study shows that the SOFC performance is slightly decreased with an increase in gas velocity. This is because the high gas velocity inhibits the increase in molar fractions of H_2 and CO (by DIR reaction). While for H_2-fueled SOFC, high gas velocity help sustain high molar fraction of H_2, which will otherwise decrease along the channel due to electrochemical reaction. Thus high gas velocity is beneficial to achieve high electric output for H_2-fueled SOFC, but tends to decrease the electric performance of SOFC running on hydrocarbon fuels. As expected, the current density increases considerably with decreasing operating potential. However, the chemical reaction rates are also significantly affected by operating potential. Higher current density consumes more H_2 and CO, thus favors DIR reaction and backward WGS reaction.

An alternative method is proposed to determine the open-circuit potential of SOFC running on hydrocarbon fuels considering chemical reactions in the porous anode. Different from the previous methods using the Nernst equation to calculate the open-circuit potential of H_2-fueled SOFC, the open-circuit potential of SOFC running on partially pre-reformed CH_4 fuel is determined as the potential at which the total current is zero. The open circuit potentials at 1073K and 1173K were found to be 0.937V and 0.936V, respectively. At the open circuit potential, it is found that the total current density increases considerably from a negative value near the inlet to a positive value at the outlet. This means the electricity generated in the downstream in fuel cell operation is consumed in the upstream in electrolysis mode.

Acknowledgments

This research was supported by a grant (No. A-PK48) from The Hong Kong Polytechnic University, Hong Kong.

Nomenclature

c_p	Heat capactity ($J.kg^{-1}.K^{-1}$)
d_a	Thickness of anode (μm)
d_c	Thickness of cathode (μm)
$D_{i,m}^{eff}$	Effective diffusion coefficient of species *i* in gas mixture ($cm^2.s^{-1}$)
$D_{i,k}$	Knudsen diffusion coefficient of *i* ($cm^2.s^{-1}$)
$D_{i,j}$	Binary diffusion coefficient of *i* and *j*($cm^2.s^{-1}$)
E	Equilibrium potential (V)
E_0	Reversible potential at standard condition (V)
F	Faraday constant ($9.6485x10^4$ $C.mol^{-1}$)
H_{DIR}	Heat demand for direct internal reforming of methane ($J.mol^{-1}$)
H_{WGS}	Heat generation from water gas shift reaction ($J.mol^{-1}$)
J	Current density ($A.m^{-2}$)
k	Thermal conductivity ($W.m^{-1}.K^{-1}$)
M_i	Molecular weight of species *i* ($kg.mol^{-1}$)
P	Operating pressure (bar)
P_i^I	Partial pressure (bar) of species *i* at electrode-electrolyte interface
R_{act}	Resistivity due to electrochemical reaction ($\Omega.m^2$)
R_{DIR}	Reaction rate of direct internal reforming of methane ($mol.m^{-3}.s^{-1}$)
R_{WGS}	Rate of water gas shift reaction ($mol.m^{-3}.s^{-1}$)
r_p	Mean pore radius of electrode (μm)
R	Universal gas constant (8.3145 $J.mol^{-1}.K^{-1}$)

S_i	Entropy of species *i* (*i* represents H_2O, H_2, and O_2)
S_m	Source term in continuity equation ($kg.m^{-3}.s^{-1}$)
S_x, S_y	Source terms in momentum equations ($kg.m^{-2}.s^{-2}$)
S_T	Source terms in energy equations ($W.m^{-3}$)
S_{sp}	Source terms in species equations ($kg.m^{-3}.s^{-1}$)
T	Operating temperature (K)
U	Velocity in x direction ($m.s^{-1}$)
U_{in}	Gas velocity at the SOFC inlet ($m.s^{-1}$)
V	SOFC operating potential (V); Velocity in y direction ($m.s^{-1}$)
X	Molar fraction of species *i*
Y	Mass fraction of species *i*
ε	Electrode porosity
ξ	Electrode tortuosity
$\sigma_{i,j}$	Mean characteristic length of species *i* and *j*
Ω_D	Dimensionless diffusion collision integral
ρ	Density of the gas mixture ($kg.m^{-3}$)
μ	Viscosity of gas mixture ($kg.m^{-1}.s^{-1}$)
$\eta_{act,a}$	Activation overpotential at anode (V)
$\eta_{act,c}$	Activation overpotential at cathode (V)
η_{ohmic}	Ohmic overpotential of the electrolyte (V)

References

[1] S.C. Singhal, K. Kendall, High Temperature Solid Oxide Fuel Cells – Fundamentals, Design and Applications, Elsevier, New York, 2003.
[2] A.J. Appleby, Fuel cell technology: status and future prospects, *Energy* 21(1996) 521-653.
[3] C.O. Colpan, I. Dincer, F. Hamdullahpur, Thermodynamic modeling of direct internal reforming solid oxide fuel cells operating with syngas, *International Journal of Hydrogen Energy* 32 (2007) 787-795.
[4] A.D. Hawkes, D.J.L. Brett, N.P. Brandon, Fuel cell micro-CHP techno-economics: part 2 – model application to consider the economic and environmental impact of stack degradation, *International Journal of Hydrogen Energy* 34 (2009) 9558-9569.
[5] P. Kazempoor, V. Dorer, A. Weber, Modeling and evaluation of building integrated SOFC systems, *International Journal of Hydrogen Energy* 2011, in press.
[6] Y. Shiratori, T. Ijichi, T. Oshima, K. Sasaki, Internal reforming SOFC running on biogas, *International Journal of Hydrogen Energy* 35 (2010) 7905- 7912.
[7] T.S. Zhao, K.-D. Kreuer, Trung Nguyen, *Advances in Fuel Cells,* Elsevier, ISBN-13: 978-0-08-045394-1, 2007.
[8] Y. Lin, R. Ran, Y. Guo, W. Zhou, R. Cai, J. Wang, Z.P. Shao, Proton-conducting fuel cells operating on hydrogen, ammonia and hydrazine at intermediate temperatures, *Int. J. Hydrogen Energy*, 35(2010): 2637-2642.
[9] Y. Shiratori, T. Ijichi, T. Oshima, K. Sasaki, Internal reforming SOFC running on biogas, *Int. J. Hydrogen Energy*, 35 (2010): 7905- 7912.
[10] G.K. Gupta, A.M. Dean, K. Ahn, R.J. Gorte, Comparison of conversion and deposit formation of ethanol and butane under SOFC conditions, *J. Power Sources*, 158 (2006): 497-503.
[11] D. Mogensen, J.D. Grunwaldt, P.V. Hendriksen, K. Dam-Johansen, J.U. Nielsen, Internal steam reforming in solid oxide fuel cells: status and opportunities of kinetic studies and their impact on modeling, *J. Power Sources* 196(2011) 25-38.
[12] S.H. Chan, O.L. Ding, Simulation of a solid oxide fuel cell power system fed by methane, *Int. J. Hydrogen Energy*, 30 (2005): 167-179.
[13] R.T. Leah, N.P. Brandon, P. Aguiar, Modelling of cells, stacks and systems based around metal-supported planar IT-SOFC cells with CGO electrolytes operating at 500-600^{o}C, *J. Power Sources*, 145 (2005): 336-352.
[14] F. Mueller, F. Jabbari, R. Gaynor, J. Brouwer, Novel solid oxide fuel cell system controller for rapid load following, *J. Power Sources*, 172 (2007): 308-323.
[15] E. Achenbach and E. Riensche, Methane/steam reforming kinetics for solid oxide fuel cells, *J. Power Sources*, 52 (1994): 283–288.
[16] H. Zhu and R.J. Kee, A general mathematical model for analyzing the performance of fuel-cell membrane-electrode assemblies, *J. Power Sources*, 117 (2003): 61–74.
[17] P. Aguiar, C.S. Adjiman, N.P. Brandon, Anode-supported intermediate temperature direct internal reforming solid oxide fuel cell. I: model-based steady-state performance, *J. Power Sources*, 138 (2004): 120-136.
[18] H. Yakabe, T. Ogiwarw, M. Hishinuma and I. Yasuda, 3-D model calculation for planar SOFC, *J. Power Sources*, 102 (2001): 144–154.
[19] P. Iora, P. Aguiar, C.S. Adjiman, N.P. Brandon, Comparison of two IT DIR-SOFC models: impact of variable thermodynamic, physical, and flow properties, steady-state and dynamic analysis, *Chemical Engineering Science*, 60 (2005): 2963-2975.

[20] V.M. Janardhanan, O. Deutschmann, CFD analysis of a solid oxide fuel cell with internal reforming: coupled interactions of transport, heterogeneous catalysis and electrochemical processes, *J. Power Sources*, 162 (2006): 1192-1202.
[21] T. Matsui, R. Kishida, J.Y. Kim, H. Muroyama, K. Eguchi, Performance deterioration of Ni-YSZ anode induced by electrochemically generated steam in solid oxide fuel cells, *J. Electrochem. Soc.*, 157 (2010): B776-B781.
[22] K. Nikooyeh, A.A. Jeje, J.M. Hill, 3D modeling of anode-supported planar SOFC with internal reforming of methane, *J. Power Sources*, 171 (2007): 601-609.
[23] J.L. Yuan, Y. Huang, B. Sundén and W.G. Wang, CFD Approach to Analyze Parameter Effects on Chemical-Reacting Transport Phenomena in SOFC Anodes, *Heat and Mass Transfer* 45 (2009) 471-484.
[24] M. Ni, Electrolytic effect in solid oxide fuel cells running on steam/methane mixture, *J. Power Sources* 196 (2011) 2027-2036.
[25] M. Ni, D.Y.C. Leung, M.K.H. Leung, Importance of pressure gradients in solid oxide fuel cell electrodes for modeling study, *Journal of Power Sources* 183(2008) 668-673.
[26] M. Ni, 2D thermal-fluid modeling and parametric analysis of a planar solid oxide fuel cell, *Energy Conversion and Management* 51(2010) 714-721.
[27] M. Ni, D.Y.C. Leung, M.K.H. Leung, Modeling of methane fed solid oxide fuel cells: comparison between proton conducting electrolyte and oxygen ion conducting electrolyte, *Journal of Power Sources* 183 (2008) 133-142.
[28] Y. Matsuzaki, I. Yasuda, Electrochemical Oxidation of H_2 and CO in a H_2-H_2O-CO-CO_2 System at the Interface of a Ni-YSZ Cermet Electrode and YSZ Electrolyte, *J. Electrochem. Soc.*, **1**47 (2000): 1630–1635.
[29] V.M. Janardhanan and O. Deutschmann, Numerical study of mass and heat transport in solid-oxide fuel cells running on humidified methane, *Chemical Engineering Science* 62 (2007) 5473–5486.
[30] M. Ni, M.K.H. Leung, D.Y.C. Leung, Mathematical modeling of proton-conducting solid oxide fuel cells and comparison with oxygen-ion-conducting counterpart, *Fuel Cells* 7 (2007) 269-278.
[31] M. Ni, M.K.H. Leung, D.Y.C. Leung, Parametric study of solid oxide fuel cell performance, *Energy Conversion and Management* 48 (2007) 1525-1535.
[32] Personal communication with Dr. M. S. Sohal from Idaho National Laboratory, at ASME 2010 8th International Fuel Cell Science, Engineering & Technology Conference, June 14-16, 2010, Brooklyn, New York, USA.
[33] S.H. Chan, K.A. Khor, Z.T. Xia, A complete polarization model of a solid oxide fuel cell and its sensitivity to the change of cell component thickness, *Journal of Power Sources* 93 (2001) 130-140.
[34] W. Lehnert, J. Meusinger and F. Thom, Modelling of gas transport phenomena in SOFC anodes, *J. Power Sources* 87 (2000) 57–63.
[35] B.A. Haberman and J.B. Young, Three-dimensional simulation of chemically reacting gas flows in the porous support structure of an integrated-planar solid oxide fuel cell, *International Journal of Heat and Mass Transfer* 47(2004) 3617-3629.
[36] M.W. Chase, NIST-JANAF thermochemical tables (4th ed.), American Chemical Society, American Institute of Physics for the National Institute of Standards and Technology, 1998.
[37] S.V. Patankar, Numerical heat transfer and fluid flow, McGraw-Hill, New York (1980).
[38] C.Y. Wang, Fundamental models for fuel cell engineering, *Chem Rev* 104 (2004) 4727–4765.
[39] R.C. Reid, J.M. Prausnitz and B.E. Poling, The properties of gases & liquids (4th ed.), McGraw-Hill Book Company, New York (1987).

[40] Q. Ye, T.S. Zhao, H. Yang, J. Prabhuram, Electrochemical reaction in a DMFC under open-circuit conditions, *Electrochemical and Solid-State Letters* 8 (2005) A52-A54.

List of Tables

List of Figures

Table 1. Parameters used in simulation

Parameter	Value
Operating temperature, T (K)	1073
Operating pressure, P (bar)	1.0
Electrode porosity, ε	0.4
Electrode tortuosity, ξ	3.0
Average pore radius, r_p (μm)	0.5
Anode-supported electrolyte:	
Anode thickness d_a (μm)	500
Electrolyte thickness, L (μm)	100
Cathode thickness, d_c (μm)	100
Height of gas flow channel (mm)	1.0
Length of the planar SOFC (mm)	20
Thickness of interconnect (mm)	0.5
Inlet velocity at anode: U_{in} ($m.s^{-1}$)	1.0
Cathode inlet gas molar ratio: O_2/N_2	0.21/0.79
Anode inlet gas molar ratio: $H_2O/CH_4/H_2/CO_2/CO$	0.493/0.171/0.263/0.044/0.029
SOFC operating potential (V)	0.8
Thermal conductivity of SOFC component ($W.m^{-1}.K^{-1}$)	
Anode	11.0
Electrolyte	2.7
Cathode	6.0
Interconnect	1.1

Table 2. Models for calculating the rates of DIR and WGS reaction in SOFC anode

Lehnert et al's model [34]	Rate of DIR reaction: R_{DIR} (mol.m^{-3}.s^{-1})	$R_{DIR} = k_{MSR}^{+} P_{CH_4} P_{H_2O} - k_{MSR}^{-} P_{CO} \left(P_{H_2}\right)^3$
	Rate of WGS reaction: R_{WGS} (mol.m^{-3}.s^{-1})	$R_{WGS} = k_{WGS}^{+} P_{CO} P_{H_2O} - k_{WGS}^{-} P_{CO_2} P_{H_2}$
Haberman and Young's model [35]	Rate of DIR reaction: R_{DIR} (mol.m^{-3}.s^{-1})	$R_{DIR} = k_{rf}\left(P_{CH_4} P_{H_2O} - \frac{P_{CO}\left(P_{H_2}\right)^3}{K_{ps}}\right)$ $k_{rf} = 2395 \exp\left(\frac{-231266}{RT}\right)$
	Rate of WGS reaction: R_{WGS} (mol.m^{-3}.s^{-1})	$R_{WGS} = k_{sf}\left(P_{CO} P_{H_2O} - \frac{P_{CO_2} P_{H_2}}{K_{ps}}\right)$ $k_{sf} = 0.0171 \exp\left(\frac{-103191}{RT}\right)$

Table 3. Governing Equations for Heat and Mass Transport in an SOFC

Continuity equation	$\frac{\partial(\rho U)}{\partial x}+\frac{\partial(\rho V)}{\partial y}=S_m$	Anode-electrolyte interface $S_m=\left(\frac{JM_{H_2O}}{2F}-\frac{JM_{H_2}}{2F}\right)\frac{A_{act}}{V_c}$ $=\frac{JM_{H_2O}}{2F\Delta y}-\frac{JM_{H_2}}{2F\Delta y}$ Cathode-electrolyte interface $S_m=-\frac{JM_{O_2}}{4F\Delta y}$
Momentum equations	$\frac{\partial(\rho UU)}{\partial x}+\frac{\partial(\rho VU)}{\partial y}=-\frac{\partial P}{\partial x}+\frac{\partial}{\partial x}\left(\mu\frac{\partial U}{\partial x}\right)+\frac{\partial}{\partial y}\left(\mu\frac{\partial U}{\partial y}\right)+S_x$ $\frac{\partial(\rho UV)}{\partial x}+\frac{\partial(\rho VV)}{\partial y}=-\frac{\partial P}{\partial y}+\frac{\partial}{\partial x}\left(\mu\frac{\partial V}{\partial x}\right)+\frac{\partial}{\partial y}\left(\mu\frac{\partial V}{\partial y}\right)+S_y$	$S_x=\frac{\mu U}{B_g}$ $S_y=\frac{\mu V}{B_g}$
Energy equation	$\frac{\partial(\rho c_P UT)}{\partial x}+\frac{\partial(\rho c_P VT)}{\partial y}=\frac{\partial}{\partial x}\left(k\frac{\partial T}{\partial x}\right)+\frac{\partial}{\partial y}\left(k\frac{\partial T}{\partial y}\right)+S_T$ In porous electrodes: $k=\varepsilon k_f+(1-\varepsilon)k_s;\ c_p=\varepsilon c_{p,f}+(1-\varepsilon)c_{p,s}$	In anode $S_T=R_{DIR}H_{DIR}+R_{WGS}H_{WGS}$ In electrolyte $S_T=-\frac{JT\Delta S}{2FL}+\frac{J\eta_t}{L}$ $\Delta S=S_{H_2O}-0.5S_{O_2}-S_{H_2}$ $\eta_t=V-E$
Species equations	$\frac{\partial(\rho UY_i)}{\partial x}+\frac{\partial(\rho VY_i)}{\partial y}=\frac{\partial}{\partial x}\left(\rho D_{i,m}\frac{\partial Y_i}{\partial x}\right)+\frac{\partial}{\partial y}\left(\rho D_{i,m}\frac{\partial Y_i}{\partial y}\right)+S_{sp}$	S_{sp} can be calculated in a way similar to S_m, with inclusion of the effect of DIR and WGS reactions in the anode.

Table 4. Parameters used in calculating the effective diffusion coefficients [39]

	CO	CO_2	H_2	O_2	CH_4	N_2	H_2O
σ_i	3.69	3.941	2.827	3.467	3.758	3.798	2.641
ε_i / k	91.7	195.2	59.7	106.7	148.6	71.4	809.1

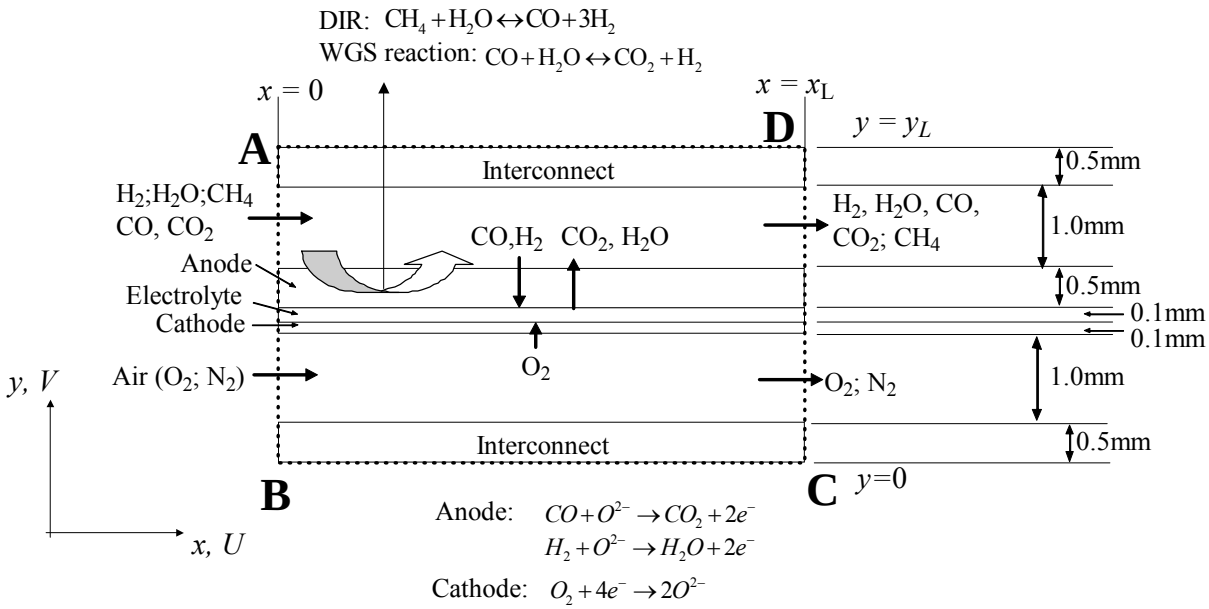
DIR: $CH_4 + H_2O \leftrightarrow CO + 3H_2$
WGS reaction: $CO + H_2O \leftrightarrow CO_2 + H_2$
$x = 0$
$x = x_L$
A
D
B
C
$y = y_L$
$y=0$
Interconnect
Interconnect
H_2;H_2O;CH_4
CO, CO_2
H_2, H_2O, CO,
CO_2; CH_4
CO,H_2 CO_2, H_2O
Anode
Electrolyte
Cathode
O_2
Air (O_2; N_2)
O_2; N_2
0.5mm
1.0mm
0.5mm
0.1mm
0.1mm
1.0mm
0.5mm
y, V
x, U
Anode: $CO + O^{2-} \rightarrow CO_2 + 2e^-$
$H_2 + O^{2-} \rightarrow H_2O + 2e^-$
Cathode: $O_2 + 4e^- \rightarrow 2O^{2-}$

Figure 1.

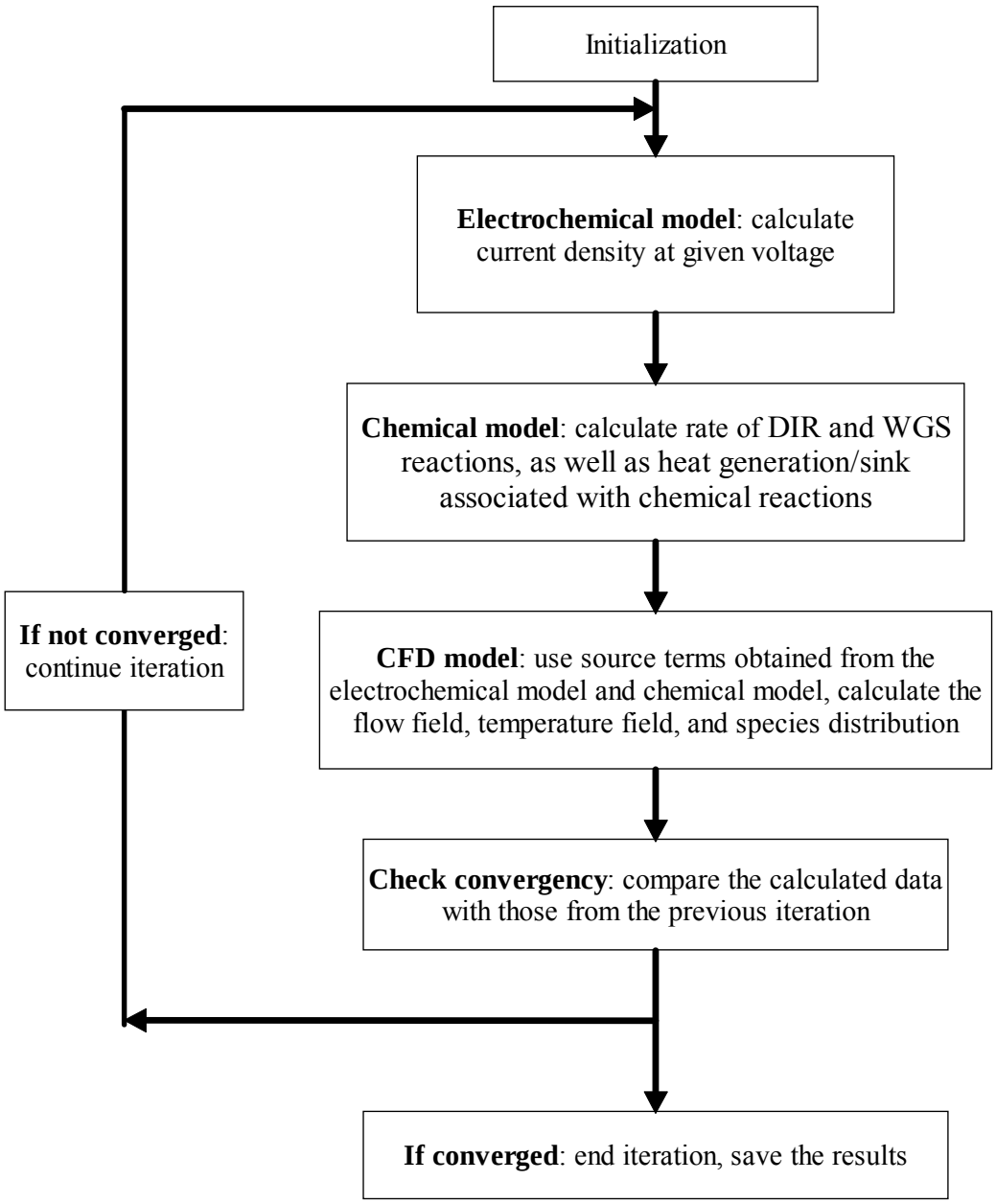
Initialization
Electrochemical model: calculate current density at given voltage
Chemical model: calculate rate of DIR and WGS reactions, as well as heat generation/sink associated with chemical reactions
CFD model: use source terms obtained from the electrochemical model and chemical model, calculate the flow field, temperature field, and species distribution
Check convergency: compare the calculated data with those from the previous iteration
If not converged: continue iteration
If converged: end iteration, save the results

Figure 2.

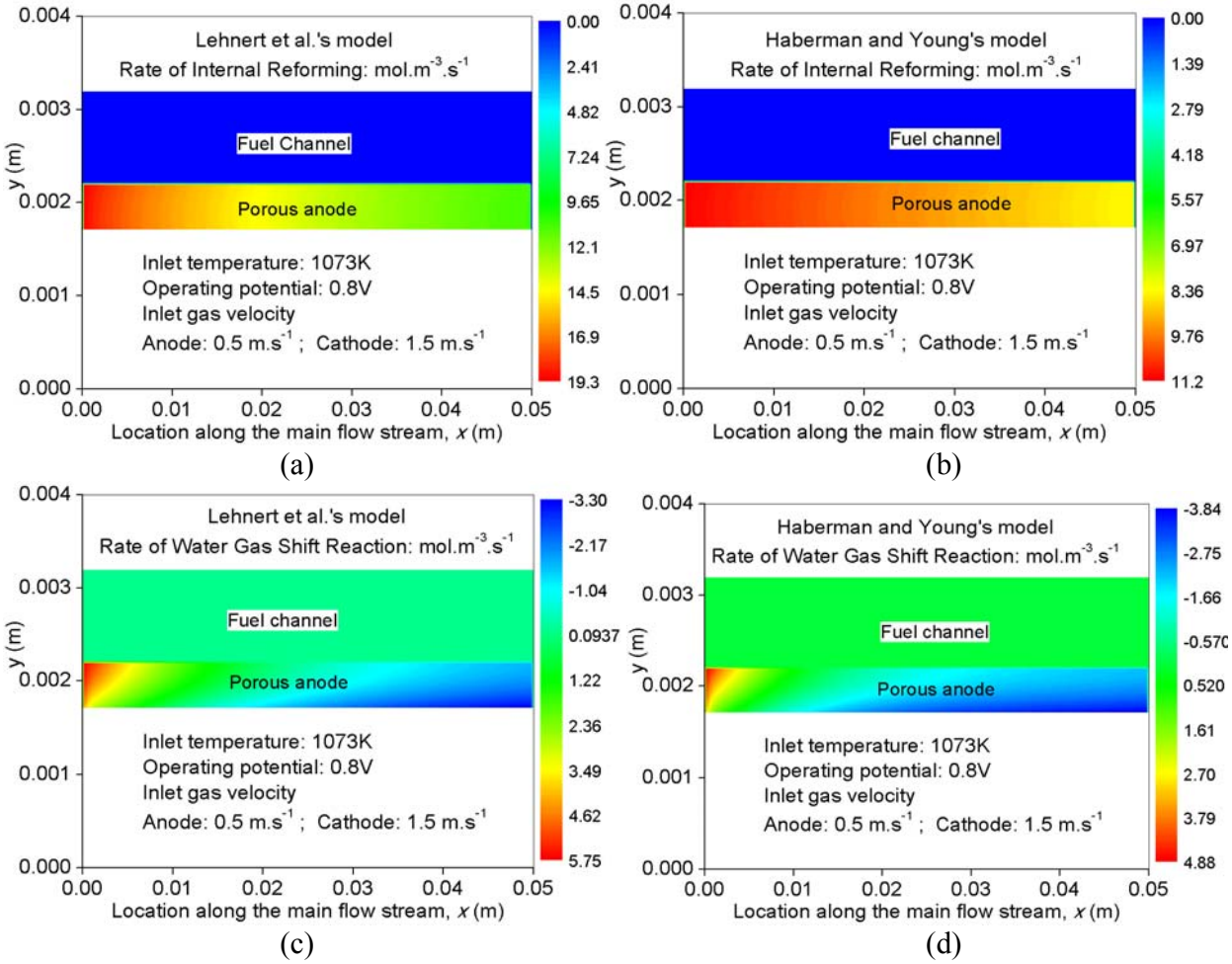
Lehnert et al.'s model
Rate of Internal Reforming: mol.m-3.s-1
Fuel Channel
Porous anode
Inlet temperature: 1073K
Operating potential: 0.8V
Inlet gas velocity
Anode: 0.5 m.s-1 ; Cathode: 1.5 m.s-1
y (m)
Location along the main flow stream, x (m)
(a)
Haberman and Young's model
Rate of Internal Reforming: mol.m-3.s-1
Fuel channel
Porous anode
Inlet temperature: 1073K
Operating potential: 0.8V
Inlet gas velocity
Anode: 0.5 m.s-1 ; Cathode: 1.5 m.s-1
y (m)
Location along the main flow stream, x (m)
(b)
Lehnert et al.'s model
Rate of Water Gas Shift Reaction: mol.m-3.s-1
Fuel channel
Porous anode
Inlet temperature: 1073K
Operating potential: 0.8V
Inlet gas velocity
Anode: 0.5 m.s-1 ; Cathode: 1.5 m.s-1
y (m)
Location along the main flow stream, x (m)
(c)
Haberman and Young's model
Rate of Water Gas Shift Reaction: mol.m-3.s-1
Fuel channel
Porous anode
Inlet temperature: 1073K
Operating potential: 0.8V
Inlet gas velocity
Anode: 0.5 m.s-1 ; Cathode: 1.5 m.s-1
y (m)
Location along the main flow stream, x (m)
(d)

Figure 3.

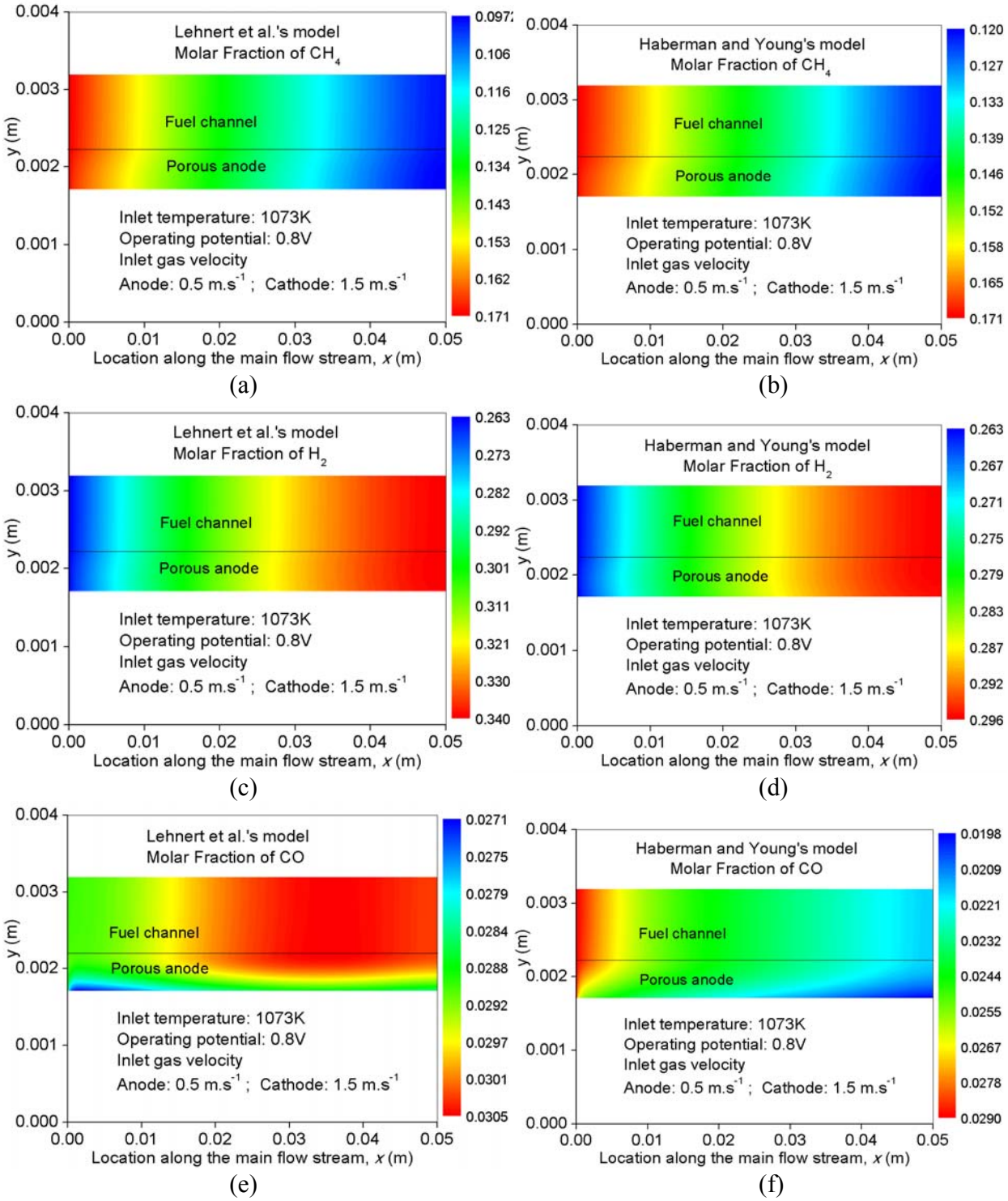
Lehnert et al.'s model
Molar Fraction of CH4
Fuel channel
Porous anode
Inlet temperature: 1073K
Operating potential: 0.8V
Inlet gas velocity
Anode: 0.5 m.s-1 ; Cathode: 1.5 m.s-1
y (m)
Location along the main flow stream, x (m)
(a)
Haberman and Young's model
Molar Fraction of CH4
(b)
Lehnert et al.'s model
Molar Fraction of H2
(c)
Haberman and Young's model
Molar Fraction of H2
(d)
Lehnert et al.'s model
Molar Fraction of CO
(e)
Haberman and Young's model
Molar Fraction of CO
(f)

Figure 4.

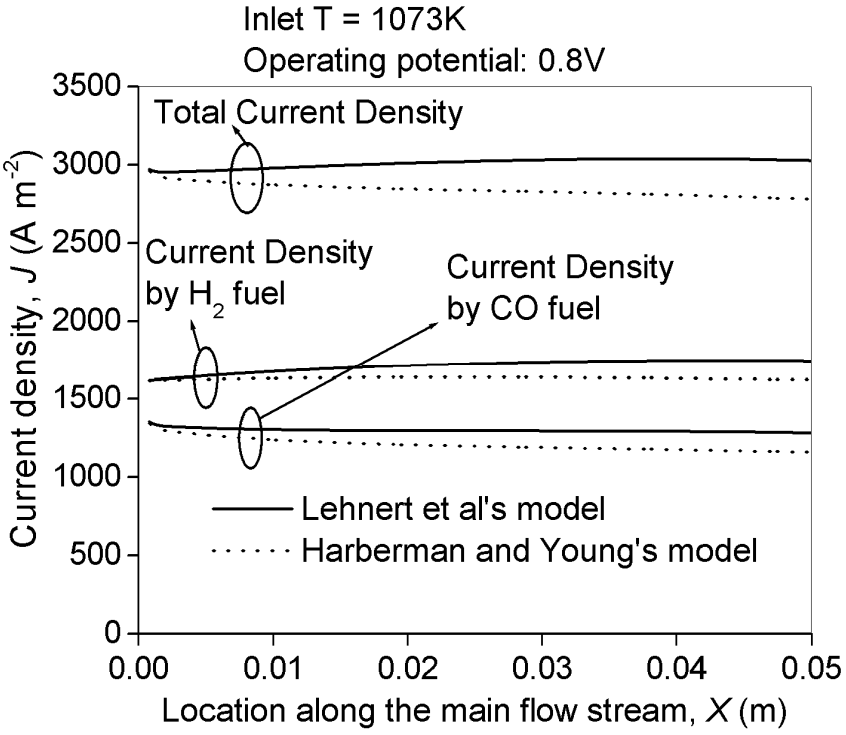
Inlet T = 1073K
Operating potential: 0.8V
Total Current Density
Current Density by H_2 fuel
Current Density by CO fuel
Lehnert et al's model
Harberman and Young's model
Current density, J (A m^{-2})
Location along the main flow stream, X (m)
3500
3000
2500
2000
1500
1000
500
0
0.00
0.01
0.02
0.03
0.04
0.05

Figure 5.

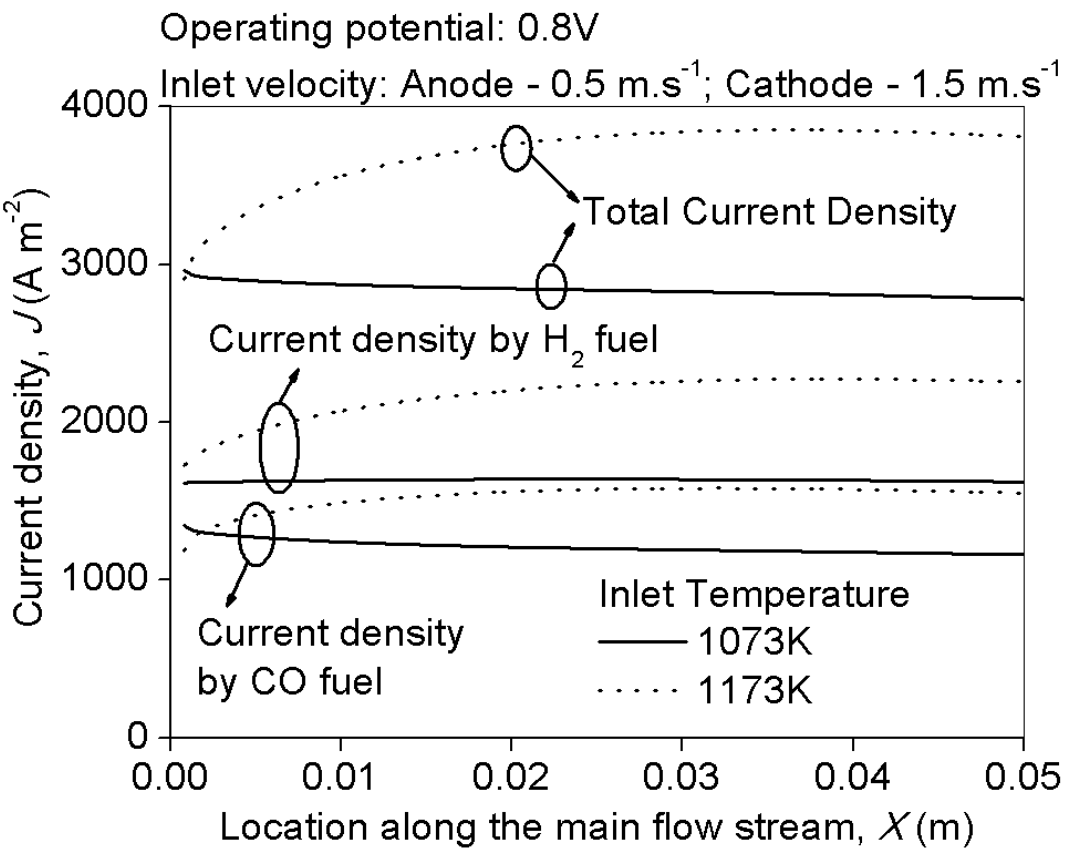
Operating potential: 0.8V
Inlet velocity: Anode - 0.5 m.s-1; Cathode - 1.5 m.s-1
Total Current Density
Current density by H2 fuel
Current density
by CO fuel
Inlet Temperature
1073K
1173K
Current density, J (A m-2)
Location along the main flow stream, X (m)
0
1000
2000
3000
4000
0.00
0.01
0.02
0.03
0.04
0.05
Figure 6

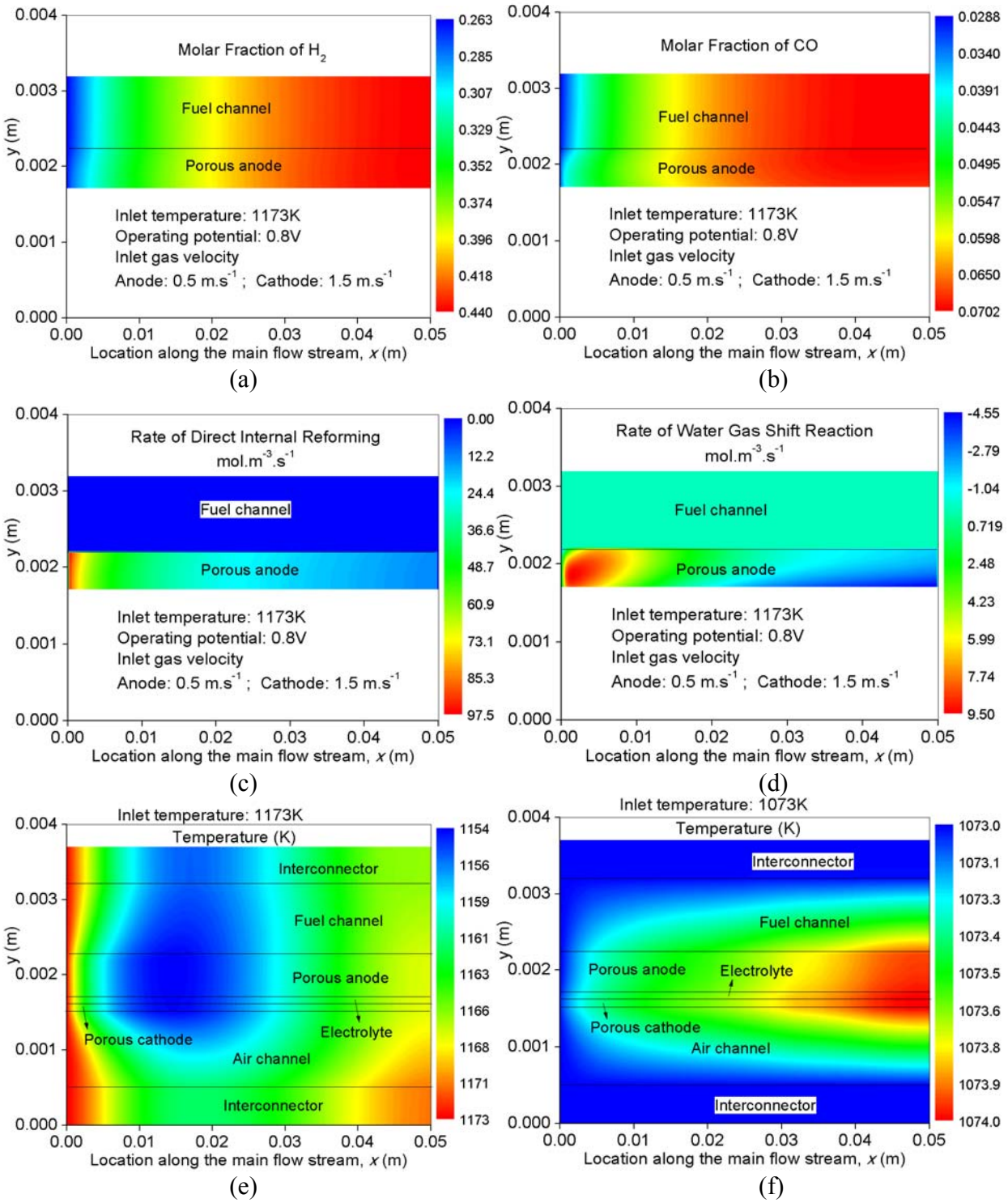
Molar Fraction of H_2
Fuel channel
Porous anode
Inlet temperature: 1173K
Operating potential: 0.8V
Inlet gas velocity
Anode: 0.5 m.s^{-1} ; Cathode: 1.5 m.s^{-1}
y (m)
Location along the main flow stream, x (m)
(a)
Molar Fraction of CO
Fuel channel
Porous anode
Inlet temperature: 1173K
Operating potential: 0.8V
Inlet gas velocity
Anode: 0.5 m.s^{-1} ; Cathode: 1.5 m.s^{-1}
y (m)
Location along the main flow stream, x (m)
(b)
Rate of Direct Internal Reforming
mol.m^{-3}.s^{-1}
Fuel channel
Porous anode
Inlet temperature: 1173K
Operating potential: 0.8V
Inlet gas velocity
Anode: 0.5 m.s^{-1} ; Cathode: 1.5 m.s^{-1}
y (m)
Location along the main flow stream, x (m)
(c)
Rate of Water Gas Shift Reaction
mol.m^{-3}.s^{-1}
Fuel channel
Porous anode
Inlet temperature: 1173K
Operating potential: 0.8V
Inlet gas velocity
Anode: 0.5 m.s^{-1} ; Cathode: 1.5 m.s^{-1}
y (m)
Location along the main flow stream, x (m)
(d)
Inlet temperature: 1173K
Temperature (K)
Interconnector
Fuel channel
Porous anode
Porous cathode
Electrolyte
Air channel
Interconnector
y (m)
Location along the main flow stream, x (m)
(e)
Inlet temperature: 1073K
Temperature (K)
Interconnector
Fuel channel
Porous anode
Electrolyte
Porous cathode
Air channel
Interconnector
y (m)
Location along the main flow stream, x (m)
(f)

Figure 7

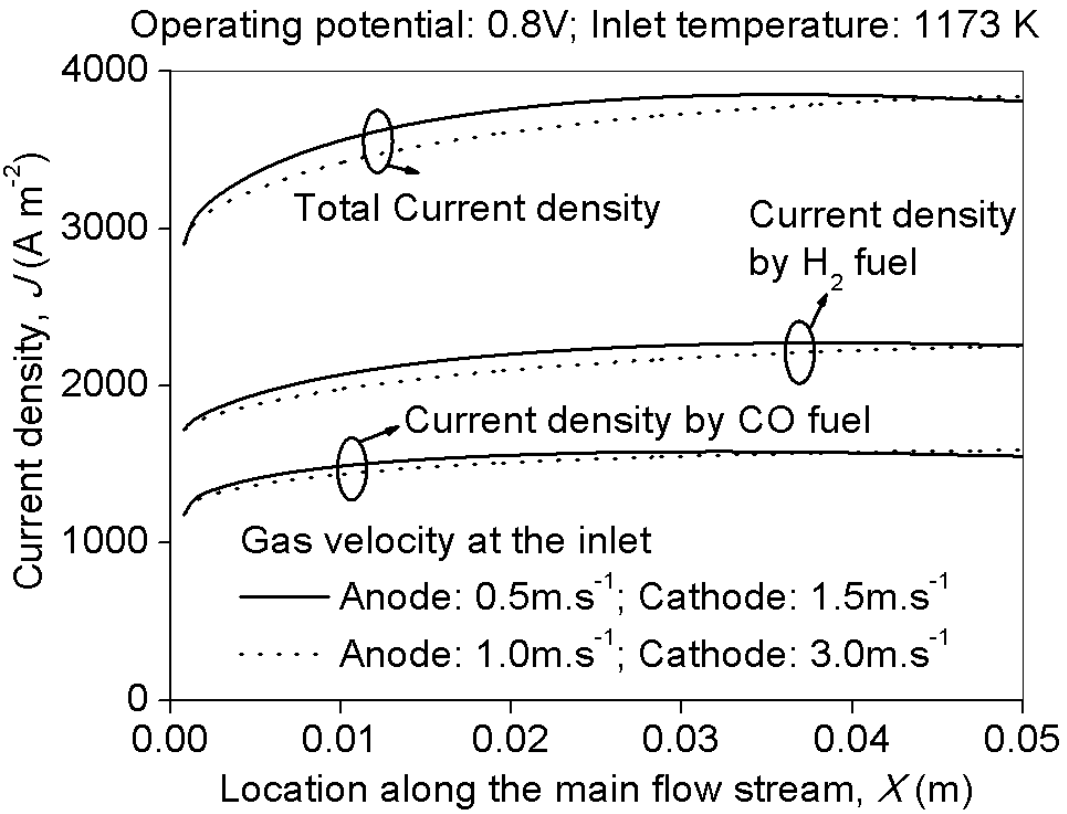
Operating potential: 0.8V; Inlet temperature: 1173 K
Current density, J (A m-2)
4000
3000
2000
1000
0
Total Current density
Current density by H2 fuel
Current density by CO fuel
Gas velocity at the inlet
Anode: 0.5m.s-1; Cathode: 1.5m.s-1
Anode: 1.0m.s-1; Cathode: 3.0m.s-1
0.00
0.01
0.02
0.03
0.04
0.05
Location along the main flow stream, X (m)

Figure 8.

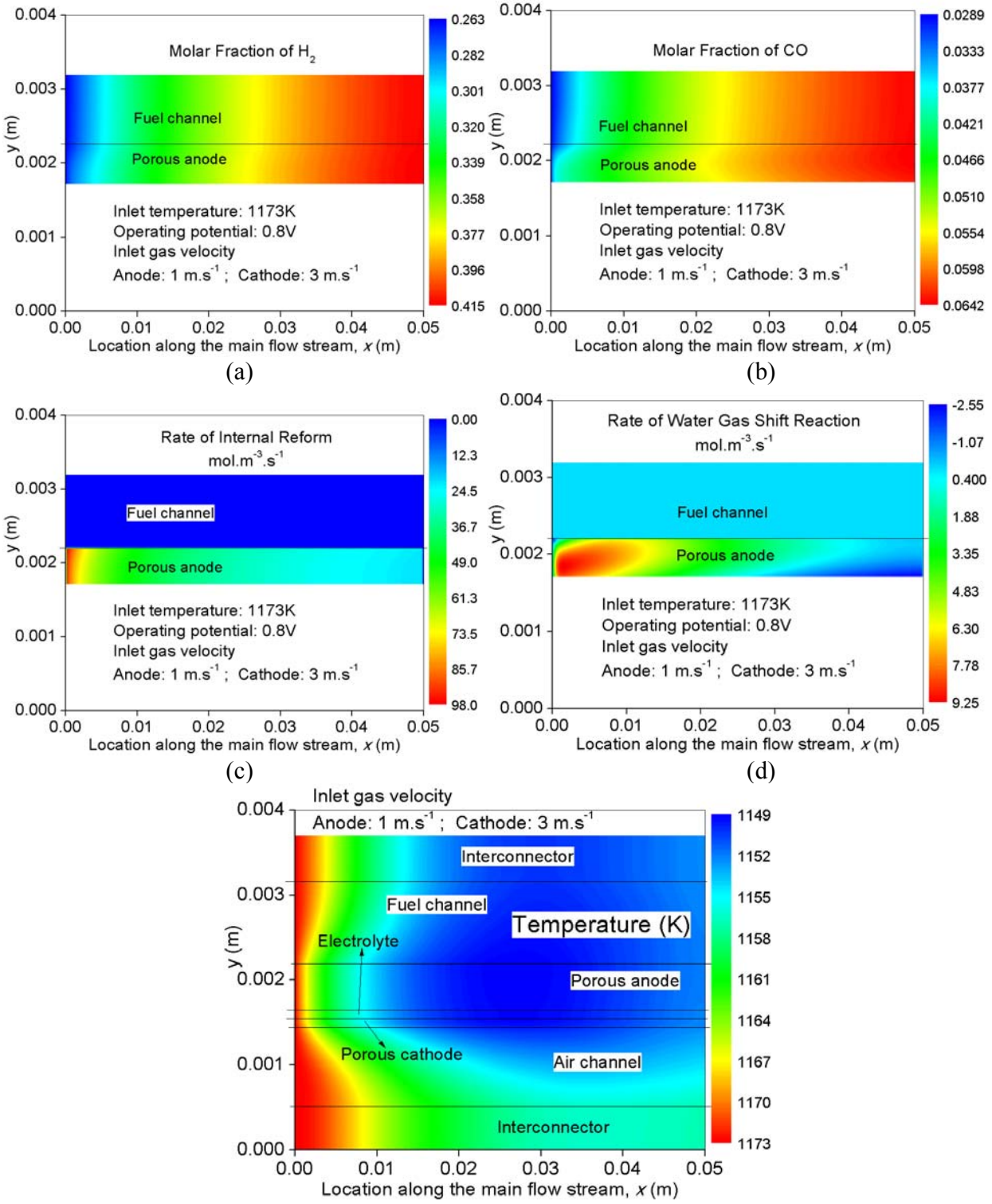
Molar Fraction of H_2
Fuel channel
Porous anode
Inlet temperature: 1173K
Operating potential: 0.8V
Inlet gas velocity
Anode: 1 m.s^{-1} ; Cathode: 3 m.s^{-1}
y (m)
Location along the main flow stream, x (m)
(a)
Molar Fraction of CO
Fuel channel
Porous anode
Inlet temperature: 1173K
Operating potential: 0.8V
Inlet gas velocity
Anode: 1 m.s^{-1} ; Cathode: 3 m.s^{-1}
y (m)
Location along the main flow stream, x (m)
(b)
Rate of Internal Reform
mol.m^{-3}.s^{-1}
Fuel channel
Porous anode
Inlet temperature: 1173K
Operating potential: 0.8V
Inlet gas velocity
Anode: 1 m.s^{-1} ; Cathode: 3 m.s^{-1}
y (m)
Location along the main flow stream, x (m)
(c)
Rate of Water Gas Shift Reaction
mol.m^{-3}.s^{-1}
Fuel channel
Porous anode
Inlet temperature: 1173K
Operating potential: 0.8V
Inlet gas velocity
Anode: 1 m.s^{-1} ; Cathode: 3 m.s^{-1}
y (m)
Location along the main flow stream, x (m)
(d)
Inlet gas velocity
Anode: 1 m.s^{-1} ; Cathode: 3 m.s^{-1}
Interconnector
Fuel channel
Temperature (K)
Electrolyte
Porous anode
Porous cathode
Air channel
Interconnector
y (m)
Location along the main flow stream, x (m)
(e)

Figure 9.

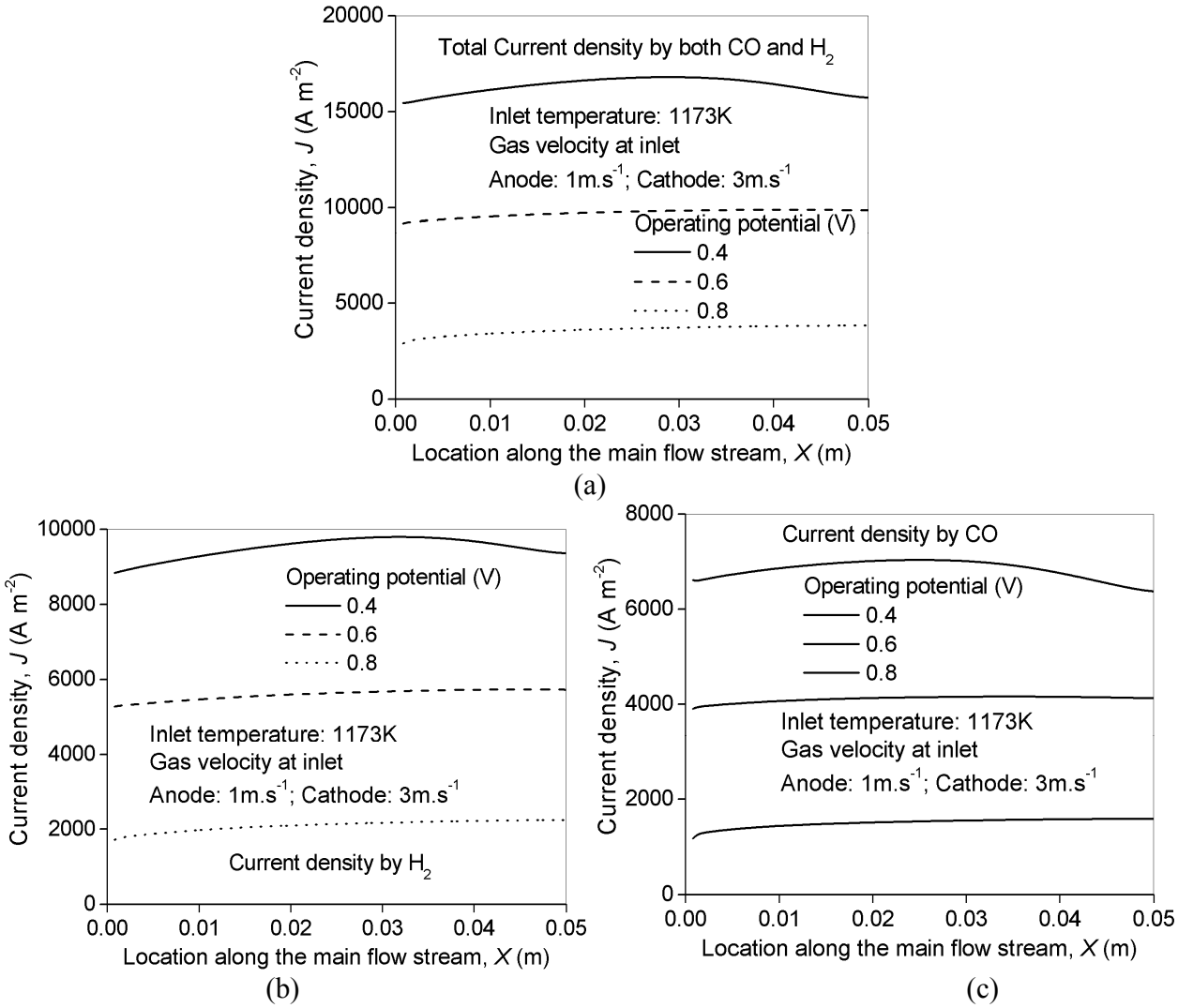
Total Current density by both CO and H2
Inlet temperature: 1173K
Gas velocity at inlet
Anode: 1m.s-1; Cathode: 3m.s-1
Operating potential (V)
0.4
0.6
0.8
Current density, J (A m-2)
Location along the main flow stream, X (m)
(a)
Current density by H2
(b)
Current density by CO
(c)

Figure 10.

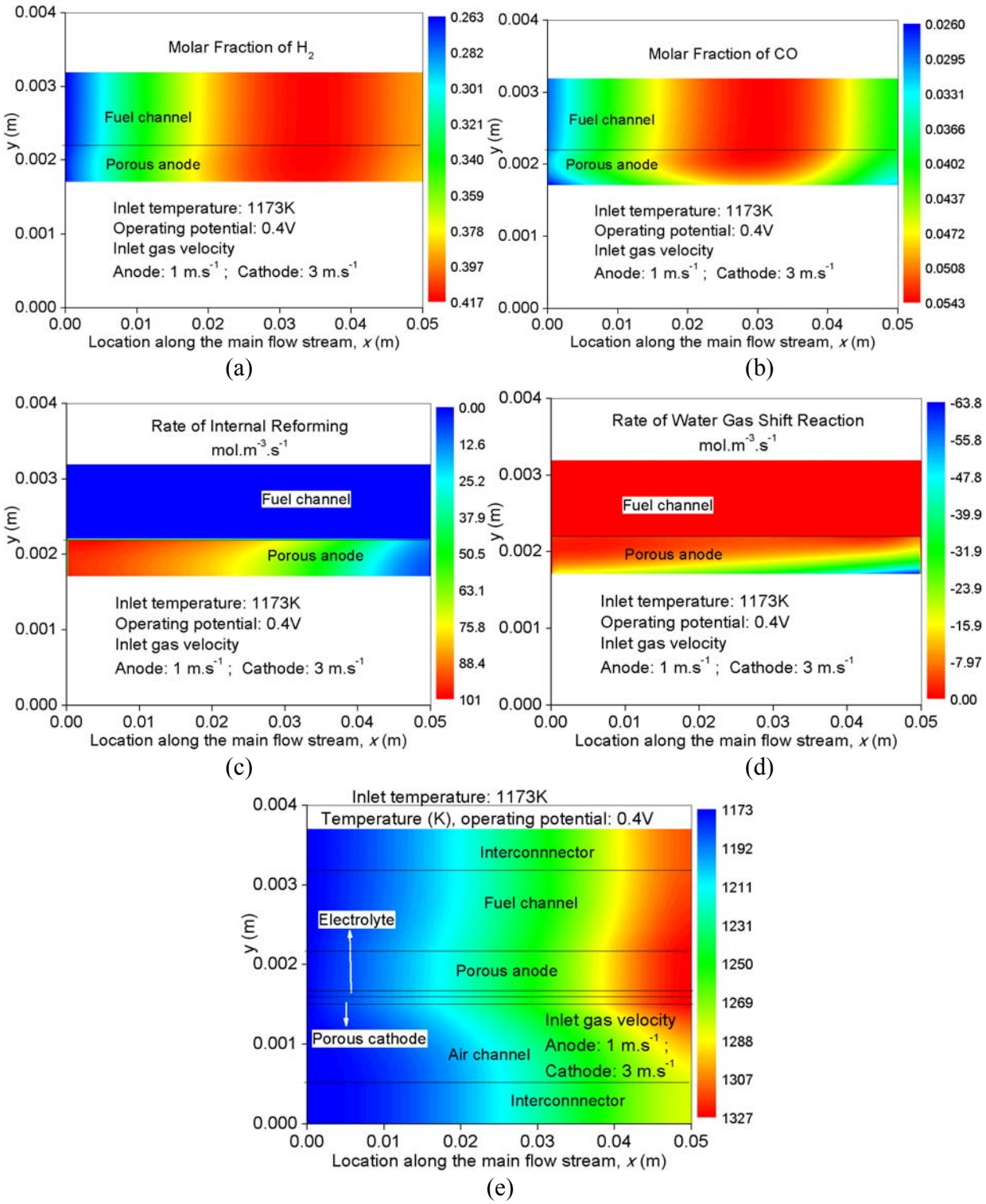
Molar Fraction of H_2
Fuel channel
Porous anode
Inlet temperature: 1173K
Operating potential: 0.4V
Inlet gas velocity
Anode: 1 m.s^{-1} ; Cathode: 3 m.s^{-1}
y (m)
Location along the main flow stream, x (m)
(a)
Molar Fraction of CO
Fuel channel
Porous anode
Inlet temperature: 1173K
Operating potential: 0.4V
Inlet gas velocity
Anode: 1 m.s^{-1} ; Cathode: 3 m.s^{-1}
y (m)
Location along the main flow stream, x (m)
(b)
Rate of Internal Reforming
mol.m^{-3}.s^{-1}
Fuel channel
Porous anode
Inlet temperature: 1173K
Operating potential: 0.4V
Inlet gas velocity
Anode: 1 m.s^{-1} ; Cathode: 3 m.s^{-1}
y (m)
Location along the main flow stream, x (m)
(c)
Rate of Water Gas Shift Reaction
mol.m^{-3}.s^{-1}
Fuel channel
Porous anode
Inlet temperature: 1173K
Operating potential: 0.4V
Inlet gas velocity
Anode: 1 m.s^{-1} ; Cathode: 3 m.s^{-1}
y (m)
Location along the main flow stream, x (m)
(d)
Inlet temperature: 1173K
Temperature (K), operating potential: 0.4V
Interconnnector
Fuel channel
Electrolyte
Porous anode
Porous cathode
Air channel
Inlet gas velocity
Anode: 1 m.s^{-1} ;
Cathode: 3 m.s^{-1}
Interconnnector
y (m)
Location along the main flow stream, x (m)
(e)

Figure 11.

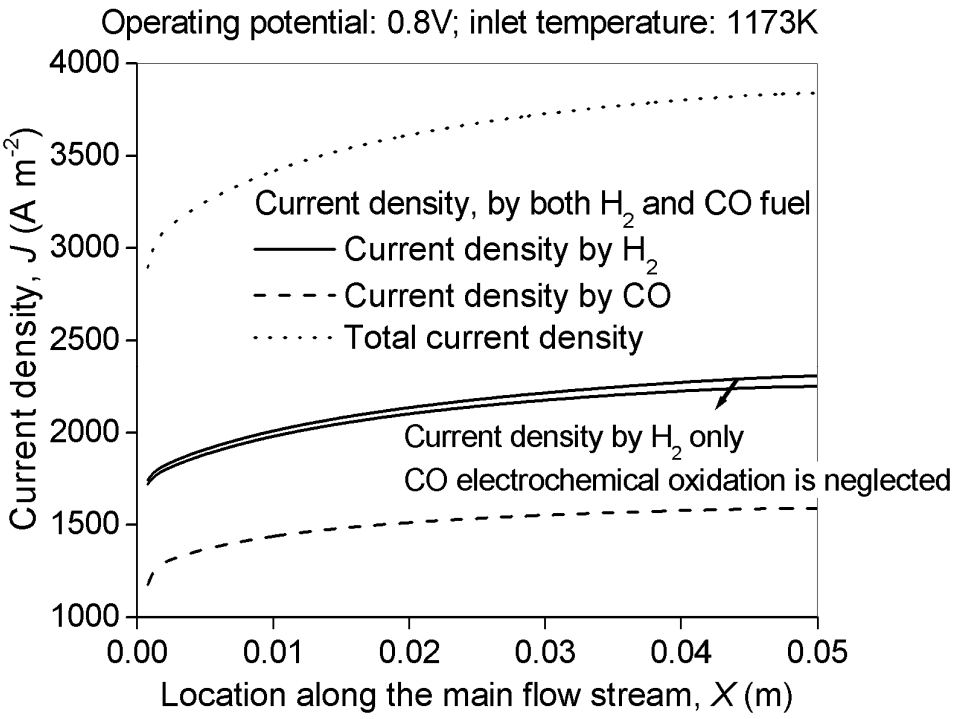
Operating potential: 0.8V; inlet temperature: 1173K
Current density, J (A m-2)
4000
3500
3000
2500
2000
1500
1000
0.00
0.01
0.02
0.03
0.04
0.05
Location along the main flow stream, X (m)
Current density, by both H2 and CO fuel
Current density by H2
Current density by CO
Total current density
Current density by H2 only
CO electrochemical oxidation is neglected

Figure 12.

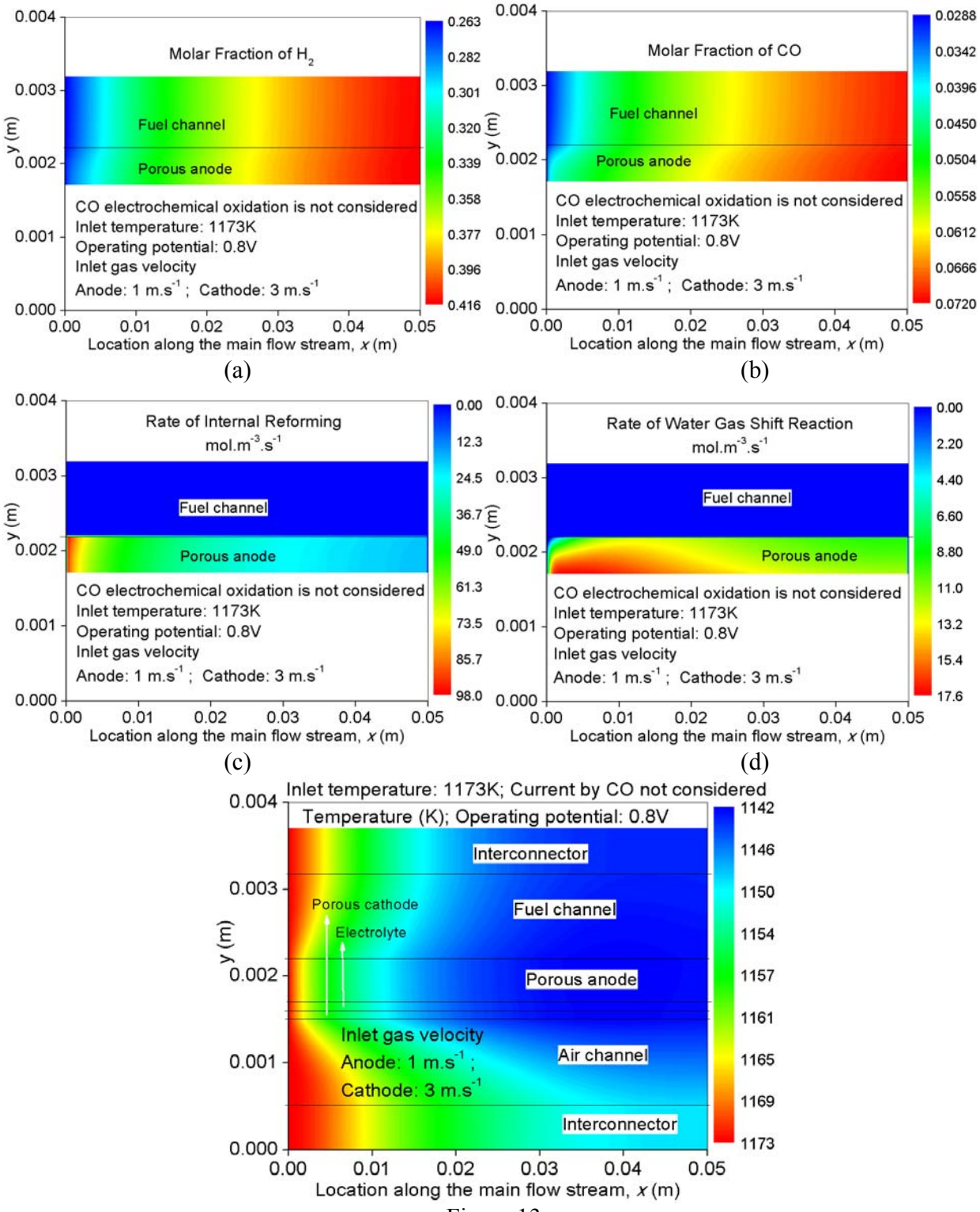
Molar Fraction of H_2
Fuel channel
Porous anode
CO electrochemical oxidation is not considered
Inlet temperature: 1173K
Operating potential: 0.8V
Inlet gas velocity
Anode: 1 m.s^{-1} ; Cathode: 3 m.s^{-1}
0.263 0.282 0.301 0.320 0.339 0.358 0.377 0.396 0.416
Location along the main flow stream, x (m)
(a)
Molar Fraction of CO
Fuel channel
Porous anode
CO electrochemical oxidation is not considered
Inlet temperature: 1173K
Operating potential: 0.8V
Inlet gas velocity
Anode: 1 m.s^{-1} ; Cathode: 3 m.s^{-1}
0.0288 0.0342 0.0396 0.0450 0.0504 0.0558 0.0612 0.0666 0.0720
Location along the main flow stream, x (m)
(b)
Rate of Internal Reforming
mol.m^{-3}.s^{-1}
Fuel channel
Porous anode
CO electrochemical oxidation is not considered
Inlet temperature: 1173K
Operating potential: 0.8V
Inlet gas velocity
Anode: 1 m.s^{-1} ; Cathode: 3 m.s^{-1}
0.00 12.3 24.5 36.7 49.0 61.3 73.5 85.7 98.0
Location along the main flow stream, x (m)
(c)
Rate of Water Gas Shift Reaction
mol.m^{-3}.s^{-1}
Fuel channel
Porous anode
CO electrochemical oxidation is not considered
Inlet temperature: 1173K
Operating potential: 0.8V
Inlet gas velocity
Anode: 1 m.s^{-1} ; Cathode: 3 m.s^{-1}
0.00 2.20 4.40 6.60 8.80 11.0 13.2 15.4 17.6
Location along the main flow stream, x (m)
(d)
Inlet temperature: 1173K; Current by CO not considered
Temperature (K); Operating potential: 0.8V
Interconnector
Porous cathode
Electrolyte
Fuel channel
Porous anode
Inlet gas velocity
Anode: 1 m.s^{-1} ;
Cathode: 3 m.s^{-1}
Air channel
Interconnector
1142 1146 1150 1154 1157 1161 1165 1169 1173
Location along the main flow stream, x (m)
y (m)

Figure 13.

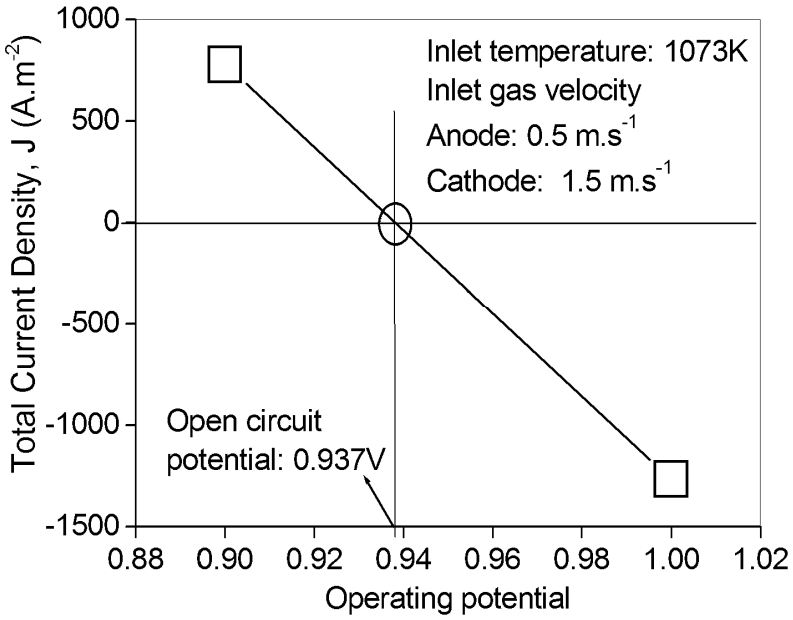
Total Current Density, J (A.m-2)
1000
500
0
-500
-1000
-1500
0.88
0.90
0.92
0.94
0.96
0.98
1.00
1.02
Operating potential
Inlet temperature: 1073K
Inlet gas velocity
Anode: 0.5 m.s-1
Cathode: 1.5 m.s-1
Open circuit
potential: 0.937V

(a)

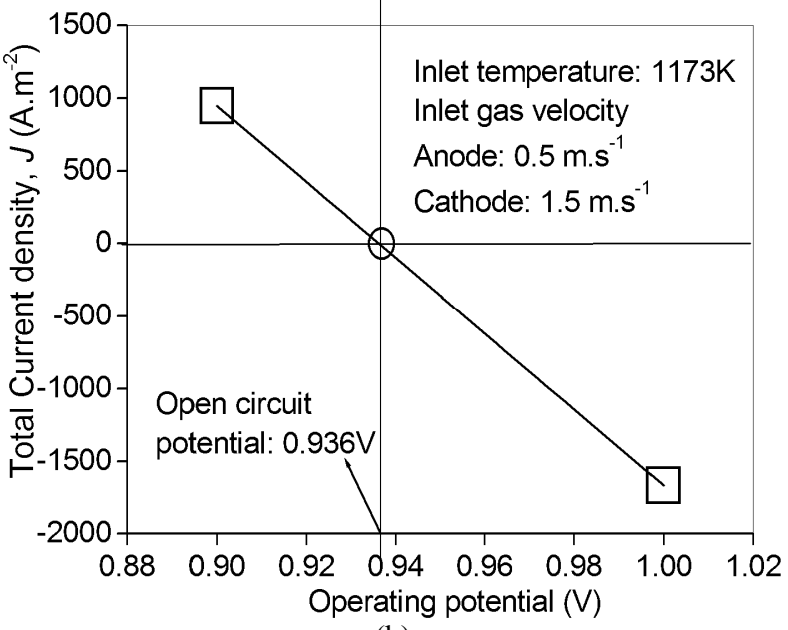
Total Current density, J (A.m-2)
1500
1000
500
0
-500
-1000
-1500
-2000
0.88
0.90
0.92
0.94
0.96
0.98
1.00
1.02
Operating potential (V)
Inlet temperature: 1173K
Inlet gas velocity
Anode: 0.5 m.s-1
Cathode: 1.5 m.s-1
Open circuit
potential: 0.936V

(b)

Figure 14.

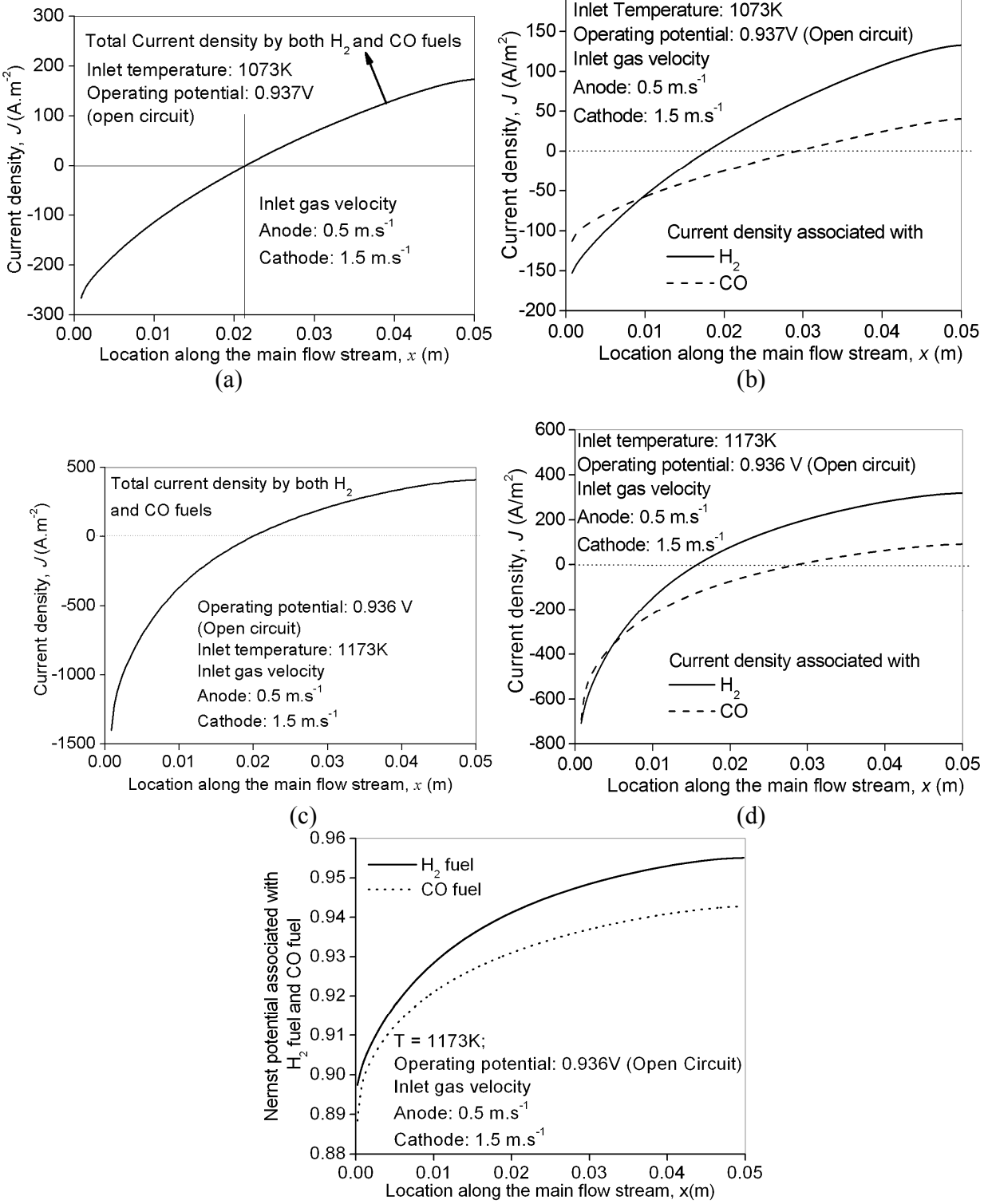
Total Current density by both H2 and CO fuels
Inlet temperature: 1073K
Operating potential: 0.937V
(open circuit)
Inlet gas velocity
Anode: 0.5 m.s-1
Cathode: 1.5 m.s-1
Current density, J (A.m-2)
Location along the main flow stream, x (m)
(a)
Inlet Temperature: 1073K
Operating potential: 0.937V (Open circuit)
Inlet gas velocity
Anode: 0.5 m.s-1
Cathode: 1.5 m.s-1
Current density associated with
H2
CO
Current density, J (A/m2)
Location along the main flow stream, x (m)
(b)
Total current density by both H2
and CO fuels
Operating potential: 0.936 V
(Open circuit)
Inlet temperature: 1173K
Inlet gas velocity
Anode: 0.5 m.s-1
Cathode: 1.5 m.s-1
Current density, J (A.m-2)
Location along the main flow stream, x (m)
(c)
Inlet temperature: 1173K
Operating potential: 0.936 V (Open circuit)
Inlet gas velocity
Anode: 0.5 m.s-1
Cathode: 1.5 m.s-1
Current density associated with
H2
CO
Current density, J (A/m2)
Location along the main flow stream, x (m)
(d)
H2 fuel
CO fuel
T = 1173K;
Operating potential: 0.936V (Open Circuit)
Inlet gas velocity
Anode: 0.5 m.s-1
Cathode: 1.5 m.s-1
Nernst potential associated with
H2 fuel and CO fuel
Location along the main flow stream, x(m)
(e)

Figure 15.